2

Computational Approaches to Cytochrome P450 Function

Sason Shaik and Samuël P. De Visser

This chapter describes computational strategies for investigating the species in the catalytic cycle of the enzyme cytochrome P450, and the mechanisms of its main processes: alkane hydroxylation, alkene epoxidation, arene hydroxylation, and sulfoxidation. The methods reviewed are molecular mechanical (MM)-based approaches (used e.g., to study substrate docking), quantum mechanical (QM) and QM/MM calculations (used to study electronic structure and mechanism).

1. Introduction

The action of cytochrome P450 (P450) enzymes has been for years a very active arena of research that led to important insights, and generated lively debates over the nature of the various species and their reactivity patterns[1]. The active species of the enzyme is based on an iron ligated to a protoporphyrin IX macrocycle and two additional axial ligands (Figure 2.1): one, called proximal, is a thiolate from a cysteinate side chain of the protein and the other, called distal, is a variable ligand that changes during the cycle. When the distal ligand becomes an oxo group, the species is called Compound I (Cpd I), which is the reactive species of the enzyme and one of the most potent oxidants known in nature.

One of the pioneering theoretical studies on Cpd I was carried out by Loew *et al.*[2], using an empirical QM method to calculate electronic structure and derive the Mössbauer parameters for the species. However, it was only after the development of density functional theoretic (DFT) methods that QM theory came of age and offered a tool that combines reasonable accuracy with speed. More recently, even better tools became available when DFT calculations were combined with MM approaches, leading to hybrid QM/MM methods that enable the study of active species in their native protein environment. All these developments have had a considerable impact on the field and an ever-growing surge of theoretical activity. It was therefore deemed timely to review the results and insights provided by these methods. The chapter starts with a very brief summary of the theoretical methods, and follows with a description of the various species in the catalytic cycle and the main mechanisms by which the reactive species of the enzyme transfers oxygen into organic compounds. As a matter of policy, the main emphasis of the chapter is on QM-based methods; while other methods are mentioned, they receive less coverage.

2. Methods

The recent monograph of Cramer[3] provides an excellent exposition of the theoretical methods,

Sason Shaik and Samuël P. De Visser • Department of Organic Chemistry and the Lise-Meitner-Minerva Center for Computational Quantum Chemistry, The Hebrew University of Jerusalem, 91904 Jerusalem, Israel.

Cytochrome P450: Structure, Mechanism, and Biochemistry, 3e, edited by Paul R. Ortiz de Montellano
Kluwer Academic / Plenum Publishers, New York, 2005.

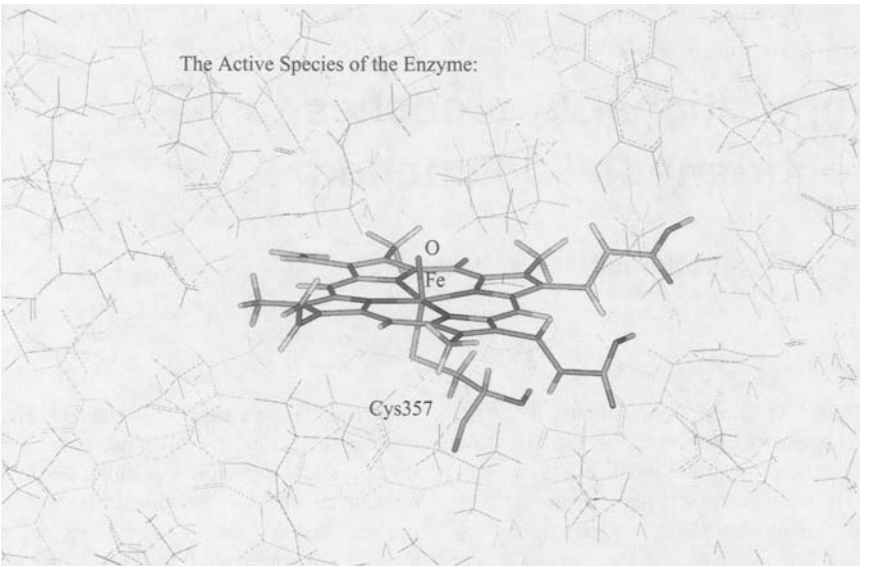

Figure 2.1. The active site of Cytochrome P450, showing Cpd I.

and the interested reader may consult this book for further details than the meager summary given here. There are three generic theoretical categories: *ab initio* methods, semiempirical methods, and MM methods. Both *ab initio* and semiempirical methods derive from QM theory; they provide electronic structure information and can be applied to the study of complete reaction pathways. By contrast, MM is a classical method: it provides only three dimensional structures and energies, and is limited to the study of related structures, for example, conformers. In *ab initio* methods, once one selects a basis set (a set of functions) that describes the atomic orbitals of the atoms in the molecule, the functional (in DFT) and everything else is calculated starting from scratch; DFT is such an approach. Semiempirical methods calculate part of the terms while others are imported from "appropriate" experimental data. MM too, uses a mix of empirical and theoretically calibrated data (e.g., force constants, atomic size parameters, strain energies, van der Waals parameters, etc.) to calculate the energy as a function of geometry, and the parameters are usually system specific, for example, to proteins, hydrocarbons, etc. As a crude generalization, there is an inverse relationship between the speed of the method and its reliability/accuracy, such that the *ab initio* methods, which are the most time consuming, are generally the most accurate, while MM is the fastest and also the least accurate.

The *ab initio* methods are split into two parts: the wave mechanical approaches and the DFT methods. In the wave mechanical approach, one starts with the Schrödinger equation and minimizes the energy by optimizing the orbitals in a wave function that represents the system at a certain level of accuracy; the latter is defined by the degree of coverage of electronic correlation. The resulting wave function defines a specific electronic state, characterized by certain orbital occupation, total spin and energy, from which all the properties of the molecule can be derived. The lowest *ab initio* level, called Hartree-Fock, describes the wave function by a single determinant built from doubly occupied orbitals, and as such does not include electron correlation. This method fails completely for transition metal containing molecules, which require multideterminantal methods that incorporate static and dynamic electron correlation, such as the complete active space self consistent field (CASSCF) method and its further augmentation by second-order perturbation theory, the CASPT2 method that also incorporates dynamic electron correlation, or the CCSD(T) method that corresponds to

coupled cluster with single and double excitations and perturbative triple excitations. At the time of writing this chapter, CASSCF, CASPT2, and CCSD(T) methods are still too time consuming for P450 species, if one wishes to optimize the geometries of the species or to trace their potential energy surfaces for a given reaction[4].

DFT methods also use a wave function, but this wave function serves merely to obtain the electron density of the molecule, and it is from the density that the energy and all molecular properties are subsequently derived. Even though the auxiliary wave function in DFT has a single determinant form, the energy expression extracted from it incorporates static as well as dynamic electron correlation. Consequently, the DFT procedure is faster than the *ab initio* procedures; its time consumption scales like Hartree-Fock theory, but its accuracy is much better, and is sometimes competitive even with CASPT2[4]. As such, DFT can treat systems of up to *c.*100 or more atoms and obtain results with decent accuracy for an entire potential energy surface of an enzymatic reaction.

Pure functionals with gradient correction of the density, for example, BP86, BLYP, BPW91, etc., are considered to be suitable for enzymatic species. However, much better are hybrid density functional methods, such as B3LYP or B3PW91, which can reproduce experimental enthalpies of formation within 3 kcal mol^{-1}, while the highly elaborate wave mechanical methods reproduce the same set of data within 1.6 kcal mol^{-1}. Reaction barriers are more difficult to reproduce with experimental accuracy, and here too B3LYP is considered to be better than the other DFT procedures. As such, B3LYP has become the standard method for carrying out biological and P450 related research[4]. To instill some uniformity in this chapter, many of the calculations were repeated here by us, using B3LYP with a double zeta basis set, composed of LACVP for Fe and 6-31G for all other atoms, hence LACVP(Fe)/6-31G(H,C,N,O,S). This basis set gives qualitatively reliable results for the assemblage of P450 species.

Semiempirical QM methods are also based on wave mechanics. However, unlike the *ab initio* methods, here many of the terms are not calculated but taken from some empirical data, which are further recalibrated to fit a set of properties. In principle, semiempirical methods provide the same information as *ab initio* methods with the exception of accuracy. The current method that can be employed for transition metal compounds is SAM1 that is based on the older AM1 method. While the method seems to be very good for zinc compounds, it is still inaccurate for many of the transition metals. Another semiempirical method used for spectroscopic properties is INDO/S/CI that also includes configuration interaction (CI). These semiempirical methods are very fast and can be used for very large systems, but their accuracy remains questionable.

MM expresses the total energy of a molecular system as a sum of bond energy terms, electrostatic terms, and van der Waals interactions. The bond energy terms include bond stretching angular deformation, and torsional deviation that are evaluated based on a force-field derived from parameters calibrated for these bond types. The electrostatic interactions involve classical electrostatics; for proteins, usually, the partial charges are kept fixed during the calculations. The van der Waals interactions involve a Lennard–Jones potential with $1/r^6$ and $1/r^{12}$ terms for the interaction energy. Since MM calculations are cheap, they can be used to run molecular dynamics (MD) calculations to study multiple conformations, as well as to map and sample an entire potential energy surface and to determine free energies. The dynamics is calculated according to Newton's laws of classical mechanics. However, due to the dimensionality of the problem, there are many algorithms for running dynamics and for sampling the configuration space. These MM calculations require computer resources and can be applied to large systems, such as enzymes and proteins. Thus, MM and MD studies are useful for the studies of large systems, in which one, for instance, explores the entrance and exit channels of substrates/products into an enzyme[5, 6] and the preferred location of substrate binding[7, 8]. By contrast, the electronic structures of all species of P450 involve unpaired electrons, different spin states, and unusual mixed-valent states, which can be studied only with QM methods.

The QM/MM method combines the advantages of QM and MM. In QM/MM calculations, the system is divided into two subsystems that are treated at different levels. The small subsystem involves the active species that is computed with a QM method such as a semiempirical or DFT.

The larger subsystem is the protein, which does not actively take part in the studied reaction, but influences the active species by providing an electrostatic field and a hydrogen bonding machinery, as well as a sterically constrained matrix with van der Waals interactions. The protein subsystem is considered to be "classical" and is treated with MM. The interactions between the QM and MM subsystems are split into electrostatic and van der Waals types. The electrostatic interactions are incorporated into the QM calculations by embedding the MM charges into the QM Hamiltonian; in this manner, the QM subsystem undergoes polarization in response to the electric field and hydrogen bonding machinery of the protein environment. The van der Waals interactions are treated classically. QM/MM calculations that involve DFT for the QM subsystem are still very demanding and elaborate, and, at the time of writing this chapter, are limited to a few species of P450. Moreover, the method is still limited to QM/MM geometry optimization, but cannot yet be used for proper sampling of configuration space, which is required in order to derive free energy quantities.

3. The Catalytic Cycle of P450

The enzyme cytochrome P450 operates by means of a catalytic cycle[9] that is schematically depicted in Figure 2.2, where the cysteinate proximal ligand is abbreviated as L, and the porphyrin macrocycle is symbolized by the two bold lines flanking the iron. The cycle follows a beautiful chemical logic that highlights the impact of chemistry on the field. The resting state of the enzyme is the ferric (Fe^{III}) complex (**1**) that possesses a water molecule as a distal ligand. With six coordination, the d-block orbitals of the complex are split into three-below-two molecular orbitals (MOs). Consequently, the five d-electrons of the complex occupy the lower MOs leading to a low-spin (LS) species. The entrance of the substrate (RH) into the protein pocket displaces the water molecule and generates the five-coordinated ferric species (**2**). The result is that the iron pops out of the plane of the porphyrin, and thereby weakens the interaction of the d-orbitals with the ligands, resulting in a narrow d-block. Consequently, the five d-electrons occupy the d-block in a high-spin (HS) fashion, and the complex itself becomes a good electron acceptor. This triggers a one-electron transfer from the reductase domain that reduces **2** to the HS ferrous (Fe^{II}) complex **3**. Ferrous porphyrin is a good dioxygen binder, and this leads to the binding of molecular oxygen to produce the LS ferrous-dioxygen complex, **4**. The latter species is again a good electron acceptor and this causes another electron transfer from the reductase to give rise to the twice-reduced ferric-dioxo species (**5**). The ferric-dioxo complex is now a good Lewis base, and therefore undergoes protonation to yield the ferric peroxide complex **6** that is also referred to as Cpd 0. Since Cpd 0 is still a good Lewis base, it undergoes a second protonation and releases a water molecule leading to the reactive species **7**, which is a high-valent iron-oxo complex also known as Cpd I. Cpd I, in turn, transfers the distal oxygen atom to the substrate, which is released and is replaced by a water molecule to regenerate the resting state of the enzyme (**1**). Alternative species, such as the $Fe–OH_2–O^-$ intermediate[10] and Cpd II that results from the one-electron reduction of Cpd I (ref. [11]), have been suggested to participate in the cycle. However, as of now there is no experimental evidence for the existence of these intermediates in the P450 cycle itself, albeit Cpd II is well known for related heme enzymes[12].

There are two additional key features in the cycle. First is the good electron donor ability of the proximal thiolate ligand, which is thought to have a significant impact on the entire cycle, and especially on the generation of Cpd I. This property of the thiolate is also called the "push effect"[13]. A second important feature that controls the efficacy of the cycle is the hydrogen-bonding interaction in the proximal side with the thiolate ligand in the cysteine loop. Thus, as shown by Poulos[14] and subsequently by Schlichting *et al.*[15], in $P450_{cam}$ the sulfur ligand is hydrogen bonded to three amidic hydrogens due to the side chains, Gln_{360}, Gly_{359}, and Leu_{358}, while a fourth hydrogen bond is donated by Gln_{360} to the carbonyl group of the cysteine. These hydrogen-bonding interactions are implicated in the stability of the enzyme and are thought to have an effect on the generation of Cpd I from Cpd 0. Other interactions in the distal side, for example, with Thr_{252} and Asp_{251}, are implicated in the proton relay mechanism that leads from **5** to **7**.

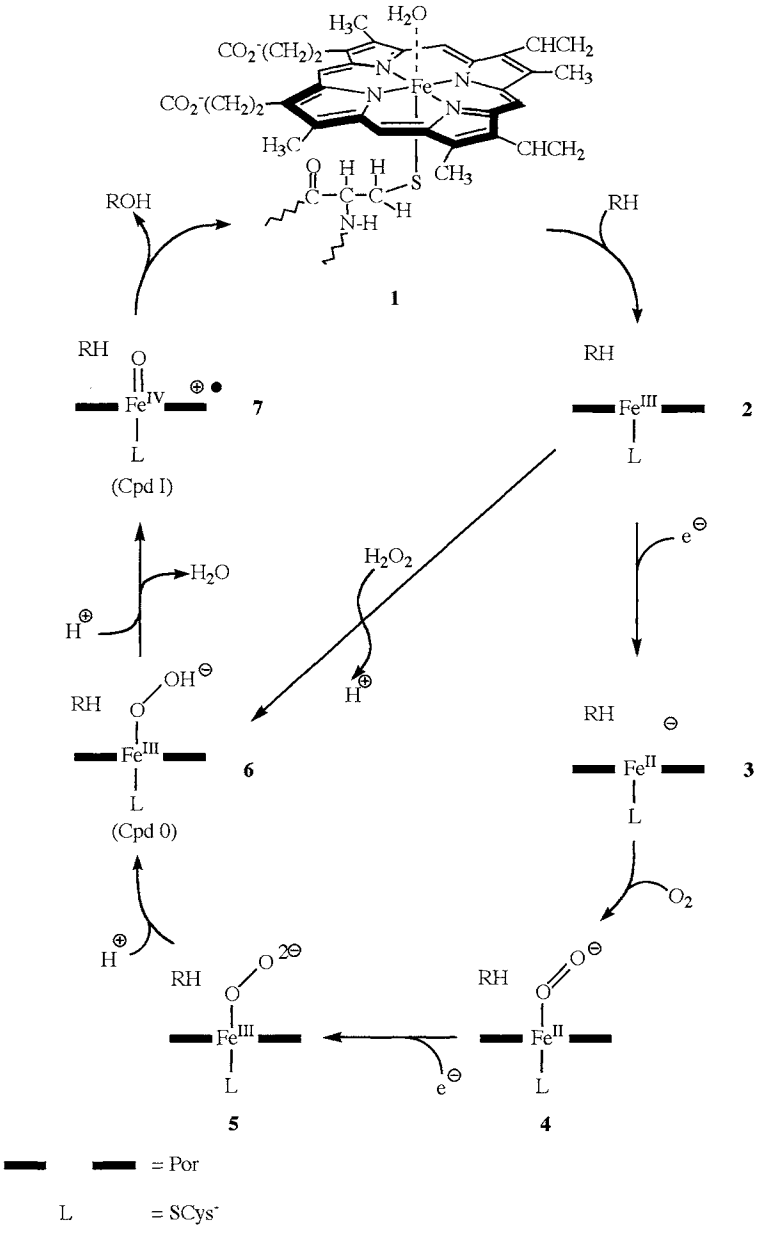

Figure 2.2. The catalytic cycle of Cytochrome P450.

The next two sections describe the results of theoretical calculations on the intermediates **1**–**7** in the catalytic cycle. Most of the literature in the field up to the year 2000 can be found in a review by Loew and Harris[16] and Loew[17]. Extensive work of Giler and Clark [18] modeled the complete catalytic cycle of P450 with methyl mercaptide (SCH_3^-) as an axial ligand using the semiempirical SAM1 method, which found good overlap between their results and experimental assignments. The five-coordinated Fe^{III} complex **2** was found to exist in a quartet ground state, whereas

the true one is a sextet. The semiempirically calculated Cpd I species is not well described, having too short an FeO bond and hence a different electronic structure compared with *ab initio* methods and experimental characterization of this species as triradicaloid. As such, we do not describe details of the semiempirical results and defer the discussion until the methods become suitable for treating iron compounds.

Each of the intermediates **1**–**7** has several closely lying spin states due to the dense orbital manifold of the iron-porphyrin system. As a typical example of the important orbitals that figure in the catalytic cycle, we depict in Figure 2.3 d-block iron and the highest lying porphyrin orbital for Cpd I (**7**). The five iron d-orbitals on the left exhibit the well-known three-below-two splitting, much like the t_{2g} and e_g sets in the purely octahedral symmetry. The three lower orbitals include the nonbonding $\delta(d_{x^2-y^2})$ orbital, which is followed by a pair of almost degenerate π^*_{FeO} (π^*_{xz} and π^*_{yz}) orbitals made from the d_{xz} and d_{yz} orbitals of iron in antibonding relationship with the ligand p_x and p_y orbitals. The upper two are σ^* orbitals that have strong antibonding relationship with the ligand orbitals; σ^*_{xy} is Fe–N antibonding, in the plane of the porphyrin ring, while $\sigma^*_{z^2}$ is antibonding along the O–Fe–S axis. Without a ligand bound to the distal position, as in **2** and **3**, or with a ligand that has only one p_π lone pair as in **6**, one of the π^* orbitals becomes a nonbonding d_{xz} orbital, while the other remains a π^*_{yz} MO and possesses antibonding interaction across the Fe–S linkage. These alternative energy orderings of the d-block orbitals, for complexes with different ligand types, are shown in the insets in Figure 2.3.

A high-lying porphyrin orbital that acquires single occupancy in some of the species is a_{2u} that is depicted in the center of Figure 2.3. In the presence of the thiolate, the a_{2u} orbital mixes strongly with the σ_S-hybrid orbital on the sulfur. The porphyrin-proximal ligand mixture of the a_{2u} orbital depends on the nature of the axial ligand. In contrast to thiolate that mixes strongly, an imidazole axial ligand mixes weakly with the porphyrin a_{2u} orbital. Finally, an orbital that may play a role is the p_π-type sulfur lone pair depicted in the far right of the diagram and is labeled π_S.

Generally, QM modeling cannot describe the complete enzyme, and one needs to truncate models that mimic faithfully the active species. Most of these models truncate the side chains on the porphyrin and use porphine, while the proximal ligand is truncated either to thiolate (SH^-), methyl mercaptide (SCH_3^-), or to cysteinate anion ($CysS^-$). The experience is that SH^- gives results closer to reality than the methyl mercaptide (SCH_3^-) ligand as revealed by QM/MM calculations[19]. This choice is due to the hydrogen-bonding machinery that stabilizes the thiolate and decreases its donor ability.

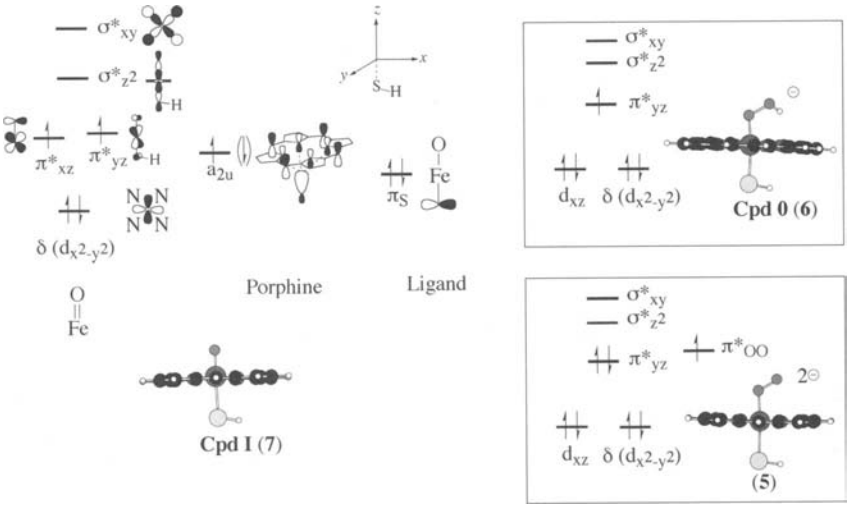

Figure 2.3. Orbital occupation of some critical species in the catalytic cycle.

To appreciate the role of thiolate in P450, it is instructive to also look at related heme-containing enzymes like HRP or catalase, where iron is coordinated to imidazole from a histidine side chain or to phenoxyl from a tyrosine side chain.

Apart from O_2 and water as ligands, calculations have been reported on other small molecules bound to iron-porphyrin complexes, among which are carbon monoxide[20] and NO[21, 22]. Calculations of metal-free porphyrin systems were reviewed by Ghosh[23] and Ghosh and Taylor[4], while DFT calculations on oxo-iron porphyrin without axial ligand[24] and studies of oxo-manganese porphyrins with different axial ligands[25] were also reported. Another complex that was studied is the hydrogen peroxide ferric complex, $Fe^{III}(H_2O_2)$, which in the P450 cycle is thought to lead to decoupling[26], while in HRP it is thought to be an intermediate in the formation of Cpd I[27, 28].

3.1. The Resting State (1)

One of the most thoroughly studied intermediates in the catalytic cycle of P450 is the resting state (**1**). Experimentally, the ferric-water complex was characterized by electron spin echo envelope modulation (ESEEM) spectroscopy and found to have a doublet ground state[29]. Based on a previous study[30] of the resting state of cytochrome *c* peroxidase (CCP), Harris and Loew[31, 32] studied the state for P450 by an early phase of the QM/MM method. They employed initial MM minimization of the X-ray structure and subsequently used INDO/ROHF/CI semiempirical methods with, and without, inclusion of the electric field of the protein in the QM procedure. The electric field-free calculations predicted that the ground state should be the sextet state, while the doublet state was found to lie significantly higher (3.84 kcal mol^{-1}). With the electrostatic field included, the doublet state descended below the sextet state by -1.59 kcal mol^{-1}. The authors concluded that the LS ground state is due to the electric field of the protein and is not an intrinsic feature of the water complex. Some support for this conclusion was provided by synthesis of a model ferric-water complex with a thiophenoxide ligand[33], which exhibits a ground state with a sextet spin, whereas the doublet state becomes the ground state only when water is replaced by a ligand with a stronger field such as imidazole.

This conclusion was contested by Green[34] who calculated the resting state of cytochrome P450 using DFT and the B3LYP functional. Green's model system had a water ligated iron-porphine and a methyl mercaptide proximal ligand. The sextet–doublet energy difference was calculated with a series of basis sets; the result was found to converge at the 6-311+G* basis set which predicted a doublet ground state. It was reasoned that the sextet state that involves the electronic configuration $\delta^1 \pi^{*1}_{xz} \pi^{*1}_{yz} \sigma^{*1}_{z^2} \sigma^{*1}_{xy}$ (Figure 2.3) is destabilized with basis set improvement, due to the increased Fe–S antibonding character of the $\sigma^*_{z^2}$ orbital. Thus, Green concluded that the doublet state is an intrinsic property of the resting state of P450.

Green's study[34], however, did not involve geometry optimization. An early DFT study by Filatov *et al.*[35], used the pure functional BP86, and partial geometry optimization. The ground state was found to be a doublet state that existed in two conformations; in the "upright" conformation, the water molecule points upward away from the porphyrin ring, while in the "tilted" conformation, the water molecule forms hydrogen bonds to the nitrogen atoms of the porphyrin ring. The water–porphyrin hydrogen bonds were found to stabilize the "tilted" complex by about 6.6 kcal mol^{-1}. Our present B3LYP/LACVP(Fe),6-31G(H,C,N,O,S) calculations, shown in Figure 2.4[36], support this conclusion, but shows that after geometry optimization, the energy differences are small, *c.*1.1 kcal mol^{-1}. An additional frequency analysis of both species showed that while the "tilted" conformation is a true minimum, the "upright" structure is a saddle point since it has one imaginary frequency, driving it back to the "tilted" form. Clearly therefore, DFT calculations indicate that the resting state has an intrinsic preference for a "tilted" conformation due to the propensity of the water ligand to undergo hydrogen bonding with a suitable acceptor. Within the protein pocket, this interaction can be supplied by the protein side chains that will stabilize the "upright" conformation, which might become the ground state or, at least be, in equilibrium with the "tilted" conformer. The ESEEM results fit better the "upright" conformation. A QM/MM study using BP86 functional for the QM subsystem was

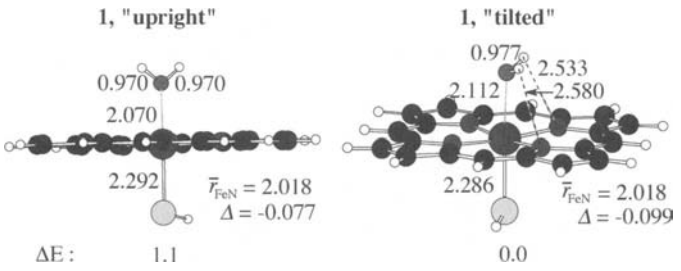

Figure 2.4. Orientations of the water ligand in the resting state (**1**). Here and elsewhere the parameter Δ specifies the deviation (in Å) of Fe from the porphyrin plane, while $r_{Fe\text{-}N}$ is an average distance of the four bonds.

performed by Scherlis *et al.*[37] and Scherlis *et al.*[38] using X-ray data without geometry optimization. The studies confirm the previous DFT findings that the doublet state is indeed the ground state. However, the study started with the "upright" conformer, so that the conformational question is still open. Future QM/MM calculations with full geometry optimization will be required to resolve this issue.

The related resting state of peroxidase enzymes, involving iron-porphine with water and imidazole as axial ligands, was studied using CASSCF(5,5) calculations[39], in which all the electronic configurations that can be generated by distributing the five d-electrons into the five d-orbitals, were included in the active space. The lowest lying state was found to be the sextet spin state with $\delta^1\ \pi^{*1}_{xz}\ \pi^{*1}_{yz}\ \sigma^{*1}_{z^2}\ \sigma^{*1}_{xy}$ configuration. The quartet and doublet states were found to be 2.21 eV (51.0 kcal mol^{-1}) and 3.41 eV (78.6 kcal mol^{-1}) higher in energy than the sextet ground state. The doublet state is characterized by short Fe–O and Fe–$N_{imidazole}$ distances of 2.09 and 2.04 Å, respectively. By contrast, the Fe–O distances in the sextet and quartet states are 2.32 and 2.34 Å, respectively. This is mainly the result of occupation of the $\sigma^*_{z^2}$ orbital which is antibonding across the O–Fe–$N_{imidazole}$ axis. These results suggested that the actual spin state would depend on the protein environment that can control the spin state by imposing bond length restriction.

Comparison of the resting states of P450 vs those of peroxidase highlights the difference between the thiolate and imidazole ligand. Thiolate mixes more strongly with the iron d-orbitals and hence the resulting $\sigma^*_{z^2}$ orbital is raised in energy, making the sextet state less favorable than the doublet. By contrast, imidazole mixes less strongly with the d-orbitals and the corresponding $\sigma^*_{z^2}$ orbital is sufficiently low to stabilize the sextet ground state by virtue of its higher exchange stabilization.

3.2. The Pentacoordinate Ferric-Porphyrin (2) and Ferrous-Porphyrin (3) Complexes

Ogliaro *et al.*[40] calculated the pentacoordinated ferric- and ferrous-porphyrin and quantified the "push effect" of the thiolate ligand, using B3LYP hybrid functional. Figure 2.5 provides optimized structures and energy separation of some of the lowest lying states. At the UB3LYP/LACV3P+* level of theory, the ground state of **2** was found to be the sextet state with $d_{x^2-y^2}{}^1\ d_{xz}{}^1\ \pi^{*1}_{yz}\ \sigma^{*1}_{z^2}\ \sigma^{*1}_{xy}$ configuration, whereas the quartet and doublet states were higher by 4.21 and 4.23 kcal mol^{-1}, respectively. Experimentally, the HS and LS forms of **2** are in equilibrium[41, 42] which suggests that their energy separation is somewhat smaller than the value predicted by the calculations, and is perhaps modulated by the electric field or steric constraints in the protein pocket. Other complications in the protein pocket are the presence of the substrate and the entropic driving force due to the expulsion of a few water molecules upon the formation of **2**. These features will have to await an appropriate QM/MM study.

Reduction of ^{6}**2** fills the $d_{x^2-y^2}$ orbital and generates a quintet ground state, ^{5}**3** for the reduced pentacoordinated ferrous complex. Another quintet state with a doubly filled d_{xz} orbital lies only 2.14 kcal mol^{-1} higher, while the triplet $d_{x^2-y^2}{}^2$

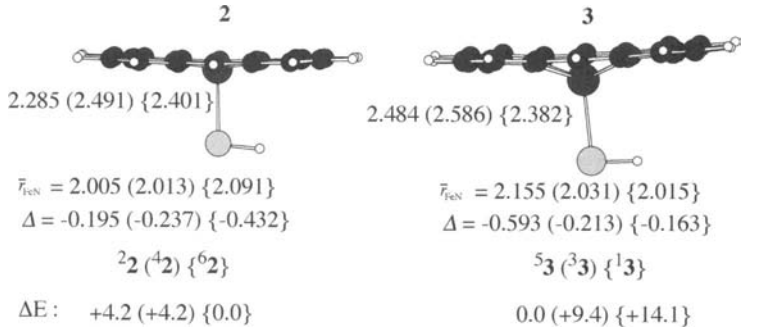

Figure 2.5. Optimized (UB3LYP/LACVP) geometries of **2** and **3**.

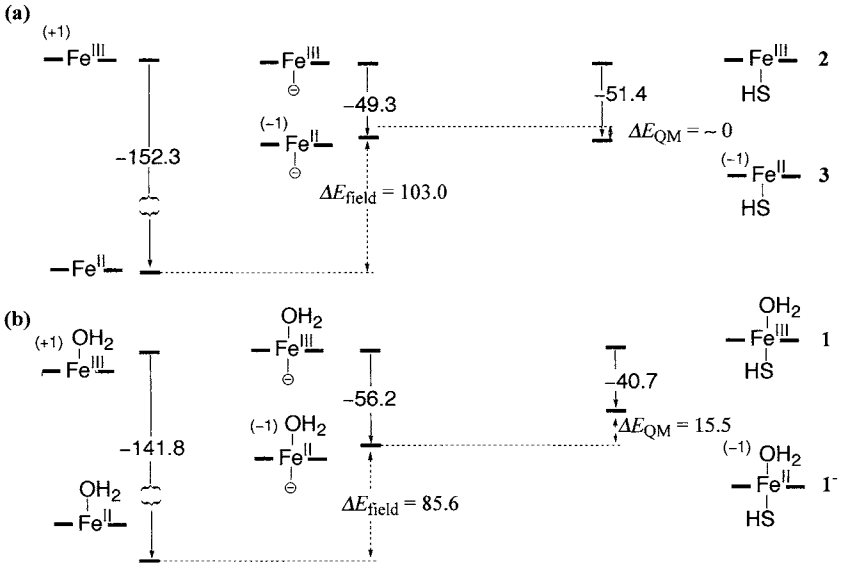

Figure 2.6. Calculated (UB3LYP/LACV3P^{+*}) push effect of the thiolate ligand (a) on the reduction energy **2** → **3**, and (b) on the reduction of **1** → **1**$^-$.

d_{xz}^2 π^{*1}_{yz} $\sigma^{*1}_{z^2}$ state lies 9.4 kcal mol^{-1} higher. The singlet state, $d_{x^2-y^2}^2$ d_{xz}^2 π^{*2}_{yz}, lies considerably above the quintet ground state by 14.1 kcal mol^{-1}.

The process ^{6}**2** → ^{5}**3** was found to be exothermic by 51.4 kcal mol^{-1} (Figure 2.6(a)), while in the absence of the thiolate ligand, the reduction energy would have been exothermic by 152.3 kcal mol^{-1}. Thus, the thiolate makes the pentacoordinated complex a much poorer electron acceptor by the "push effect" that is a measure of its electron donation capability toward the iron-porphyrin. It was reasoned[40] that since the reduction involves filling of the $d_{x^2-y^2}$ orbital, which does not mix with the thiolate orbital, this large "push effect" originates from the electrostatic interaction between the negatively charged thiolate and the iron-porphyrin moiety. To ascertain the origins of the "push effect," the thiolate was replaced by a point negative charge placed at precisely the same position as the thiolate[40]. As shown in Figure 2.6(a), the resulting reduction energy for the pseudo complex (−49.3 kcal mol^{-1}) was almost identical to the pentacoordinated complex. It was therefore concluded that during the reduction ^{6}**2** → ^{5}**3**, the "push effect" is indeed a pure electrostatic field

effect and not of quantum chemical origin. The effect of the protein electric field was estimated by embedding the bare species in a medium with a dielectric constant of $\varepsilon = 5.7$. This was found to reduce the "push effect" from 103 kcal mol^{-1} for the bare system to 33 kcal mol^{-1} for the embedded system[40]. Although significantly reduced, still the "push effect" is substantial; it makes the reduction of ^{6}**2** selective such that only the reductase can perform it and thereby trigger the initiation of the cycle.

3.3. The Gating of the Catalytic Cycle

To understand the reason why it is that only the pentacoordinated complex, **2**, and not the water complex, **1**, is reduced during the catalytic cycle, Ogliaro *et al.*[40] studied the reduction of the ferric-water complex ^{2}**1**, with and without a thiolate ligand. The results are shown in Figure 2.6(b), and project once more that without thiolate, the ferric complex is a much better electron acceptor, by *c.*101.1 kcal mol^{-1}. It was further determined by the same technique as above, that most of this energy effect (ΔE_{field}), *c.*85.6 kcal mol^{-1}, comes from the electrostatic field effect, and a small part, *c.*15.5 kcal mol^{-1} (ΔE_{QM}) is contributed by QM mixing with the p_π orbital of the thiolate ligand, which raises the electron accepting orbital π^*_{yz} (ref. [40]).

Comparison of the reduction energies in Figures 2.6(a) vs (b) reveals that the reduction of the pentacoordinated complex is more exothermic than that of the ferric-water complex by 10.7 kcal mol^{-1}. This difference safeguards the resting state against reduction by the reductase, such that a single water molecule can gate the catalytic cycle. Note however that the ligand that actually controls this gating is the thiolate; it makes all the species poorer electron acceptors, leading thereby to a selective reduction of the pentacoordinated species by the reductase. Without the thiolate ligand, all the complexes are such good electron acceptors that most reducing agents would have reduced all the species with no selectivity whatsoever. Thus, the property of a gated cycle by a single ligand (water) is achieved due to the "push effect" of the thiolate[40].

3.4. The Ferrous-Dioxygen (4) and Ferric-Dioxygen (5) Complexes

Early CASSCF calculations of a ferric-dioxygen species (**4**) with ammonia as an axial ligand were carried out by Yamamoto and Kashiwagi[43], using a minimal basis set and no geometry optimization. The lowest singlet state was found to possess a major weight of 64% of the Pauling configuration that involves coupling of Fe^{II} with the neutral O_2 moiety in its singlet situation. The state also has some $Fe^{III}O_2^-$ character due to the mixing of higher configurations.

The first DFT calculations on **4** and **5** were reported by Harris and Loew [26] and Harris *et al.*[44], using the BPW91 and BLYP pure functionals with a basis set of double-ζ plus valence polarization quality (DZVP); the two functionals gave virtually the same results, and in good agreement with experimental data. The most stable form of ferrous-dioxygen (**4**) is an end-on complex in accord with the experimental predictions[45] while the symmetrically bridged isomer was found to be much higher in energy, by *c.*28 kcal mol^{-1}. Reduction of **4** to **5** resulted in elongation of the Fe–O and Fe–S bonds, while leaving the O–O bond length intact, albeit the O–O bond order decreased from 1.20 to 0.87 (ref. [26]). In agreement with its silent ESR behavior, **4** was found to have a singlet ground state, but the triplet state to lie only 1.1 kcal mol^{-1} higher. By comparison, **5** was reported to have a doublet ground state with spin densities distributed over both oxygen atoms, in agreement with ESR data. Electronic spectra of both the ferrous- and ferric-dioxygen species, calculated with the semiempirical INDO/S/CI method[44], exhibit, in agreement with experiment, a split Soret band. The corresponding Mössbauer parameters of **4** and **5** were calculated too, and those for **4** show a good fit to experimental data.

Figure 2.7 compares the structures of ^{1}**4** and ^{2}**5** as derived by us, using the B3LYP functional with the LACVP(Fe)/6-31G(H,C,N,O,S) basis set[36], *vis-à-vis* the BPW91/DZVP results of Harris *et al.*[44] in brackets. The structures show a general fit, with the exception of **4** that appears more open in B3LYP compared with BPW91. Transformation of the DFT orbitals to natural orbitals for **4** revealed that its electronic structure is the open-shell singlet $\delta^2 d_{xz}^2 \pi^{*1}_{yz} \pi^{*1}_{OO}$ configuration.

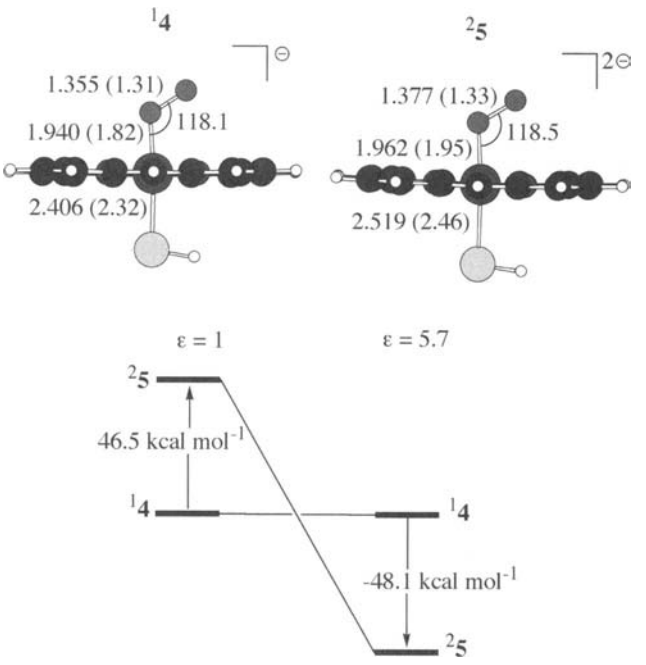

Figure 2.7. Top: optimized geometries of ^{1}**4** and ^{2}**5**. Values out of parentheses are taken from De Visser and Shaik[36], while in parentheses from Harris *et al.*[44]. Bottom: the reduction energies ^{1}**4** → ^{2}**5** (ref. [36]).

The π^*_{yz} orbital has a strong mixing with the corresponding π and π^* orbitals of the dioxygen moiety, and as such, an appropriate description of ^{1}**4** is a resonating mixture of the ferrous and ferric forms, $Fe^{II}O_2$ and $Fe^{III}O_2^-$. This conjugation requires that the dioxygen moiety, in the $Fe^{II}O_2$ form, will be in its singlet state, so that the empty π^*(O–O) orbital can mix with the doubly occupied d_{yz} (Fe) orbital; as such there is a very low lying triplet state, ^{3}**4**, only 1.1 kcal mol^{-1} higher than ^{1}**4** (ref. [44]). The electronic structure of ^{1}**4** suggests its origin from the excited singlet state of **3** and $^1\Delta_g$ state of O_2. This is further supported by the fact that **4** has low-lying HS states, for example, quintet and heptuplet states which originate from the coupling of ^{5}**3** with the triplet and singlet states of O_2. In view of the fact that both moieties of **4** have HS ground states, an interesting feature of the O_2 binding must be the spin crossover process that is yet to be properly elucidated by theory.

A natural orbital transformation analysis reveals that the odd electron in ^{2}**5** populates predominantly the π^*(O–O)-type orbital of the dioxygen ligand (Figure 2.3), as found by Harris *et al.*[44]. In reasonable agreement with Harris and Loew[26], the reduction ^{1}**4** → ^{2}**5** was found to be endothermic, by 46.5 kcal mol^{-1}. However, in the presence of an electric field modeled by a dielectric constant of ε = 5.7, the reduction energy becomes exothermic by 48.1 kcal mol^{-1}.

The effect of the protein environment on ^{1}**4** and/or ^{2}**5** was studied initially by MD simulations of $P450_{cam}$ and $P450_{eryF}$ (refs [46], [47]) using MM/MD calculations. The study showed that the ferrous-dioxygen species is stabilized by a hydrogen bond from Thr_{252} (ref. [46]). In the case of the species ^{2}**5** of $P450_{eryF}$, Harris and Loew[47] found that the distal oxygen of the twice-reduced species ^{2}**5** is linked through a hydrogen-bonding network involving neighboring amino acids, such as Ala_{241} and Ser_{246}, and several water molecules. This stable hydrogen-bonding network was implicated as the root of the double protonation that eventually converts **5** to Cpd I.

3.5. The Protonation Mechanism of Ferric-Dioxygen (5) to Cpd 0 (6)

BPW91 DFT calculations[26] showed that ^{2}**5** is an extremely strong base with a proton affinity of 422 kcal mol^{-1}, and as such it may undergo protonation by a water molecule. This study was pursued by Guallar *et al.*[48] who carried out a QM(DFT)/MM investigation of the protonation mechanism, leading from **5** to Cpd 0 (**6**) in $P450_{eryF}$. This was followed by a full quantum dynamics simulation of the proton transfer through a one-dimensional profile. The study of the QM subsystem used B3LYP with a mixed basis set, and focused on three different protonation mechanisms, by: (a) a single water molecule (W519), (b) an array of two water molecules (W519 and W564), and (c) an array of W519, W564, and an ethanol that mimics the Ser_{246} amino acid. The latter model is depicted in Figure 2.8(a), and seems to be highly conserved in many P450 isozymes that exhibit sequestered array of water molecules hydrogen bonded to a polar amino acid residue near the protein surface.

The computed energy profile[48] changed gradually from an endothermic one (+20 kcal mol^{-1}) (a) to an exothermic one (−10.7 kcal mol^{-1}) for (c) with a concomitant decrease of the barrier to 1.8 kcal mol^{-1}. The dramatic effect caused by the Grotthuss-like mechanism is very likely due to the diminishing repulsion between the doubly negative ^{2}**5** species and the incipient anion of the protonating species. Indeed, the study showed incisively that hydronium ions are not needed to initiate the protonation of the twice-reduced species, ^{2}**5**, and ruled out any putative protonation of the ferrous-dioxygen complex, ^{1}**4**, by the W519-W564-Ser_{246} array. This result is consistent with the large kinetic solvent isotope effect[50] that was observed for the reduction of ^{1}**4** to ^{2}**5**, which indicated that the reduction of ^{1}**4** and protonation of ^{2}**5** to Cpd 0, ^{2}**6**, are nearly commensurate events. The MD study[48] further showed that the initial protonation by W519 is completed within 500 fs and is the rate-determining step that triggers a sequential protonation from W564.

In a subsequent paper, Harris[51] extended the DFT study (B3LYP/ LACVP**(Fe)-6-31G*(H,C, N,O,S)) of the protonation process and analyzed its features by calculating proton affinities and transition states (TS) for protonations by various candidate acids. His studies showed, *inter alia*, that the hydronium ion can indiscriminately protonate both ^{1}**4** and ^{2}**5**, and is therefore ruled out as the source of protons. By contrast, serine, threonine, or their clusters with two water molecules (e.g., W519, W564 in $P450_{eryF}$) can protonate ^{2}**5**, but are only capable of donating a hydrogen bond to ^{1}**4**; the protonation of the HS species ^{4}**5** encounters a high barrier despite its identical proton affinity to ^{2}**5**; this was ascribed to the reduced negative charge on its distal oxygen. Using an extended array of two water molecules and alanine, the

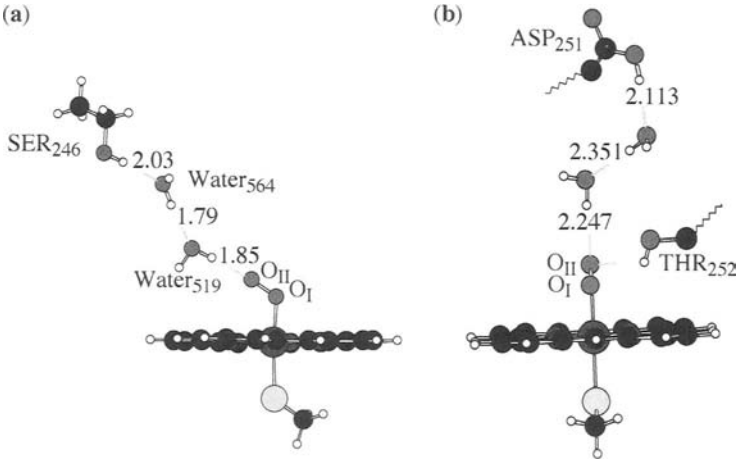

Figure 2.8. Protonation models of ^{2}**5** → ^{2}**6** taken from (a) Guallar *et al.*[48], (b) Kamachi and Yoshizawa[49].

barrier for proton transfer to ^{2}**5** was found to decrease to 1.3 kcal mol^{-1} and the product of the hydrogen-bonded array showed characteristics of low-energy hydrogen bonds that may contribute to the process facility. In this manner, the hydrogen-bonding network in the pocket creates a gentle as well as spin-state selective protonation process.

An alternative and more potent protonation mechanism was very recently studied by Kamachi and Yoshizawa[49], who calculated a model fashioned after Vidakovic *et al.*[52], with two water molecules sequestered between the acidic end, CO_2H, of Asp_{251} and the side hydroxyl group of Thr_{252}. This study involves both doublet and quartet states of **5**, and the model is shown in Figure 2.8(b) alongside the model of Guallar *et al.*[48]. The protonation is initiated by proton transfer from the CO_2H group of Asp_{251} to the adjacent water that further transfers a proton to the water molecule adjacent to the distal oxygen of ^{4,2}**5**, which completes the transfer and generates ^{4,2}**6** spontaneously. The Kamachi–Yoshizawa process was found to be much more exothermic, −61.5 (−50.1) kcal mol^{-1}, than the model of Guallar *et al.*[48], as would be expected from the stronger acid that relays the initial proton. Although barriers were also reported, one cannot avoid the conclusion that there are multiple protonation pathways that must be taken into account via QM/MM with proper sampling.

3.6. Cpd 0: The Ferric Peroxide Complex (6)

Harris and Loew[26] used BPW91 calculations and subsequently Ogliaro *et al.*[53] performed B3LYP studies of ferric peroxide, **6**, and its proximally protonated isomer, **6**-iso, shown in Figure 2.9. In both studies, **6** was found to be the stable isomer by *c.*18.4 (23.3) kcal mol^{-1} and to possess a doublet ground state, labeled $^{2}\Pi_{yz}$ (Fe^{III}), a symbol that denotes its singly occupied π^{*}_{yz} orbital[53]. An interesting feature of the ferric peroxide is the internal hydrogen bond between the hydroxo proton and the nitrogen of the porphyrin ring[53]. Application of an electric field simulated by a dielectric constant of $\varepsilon = 5.7$ further shortened the Fe–S bond and the OH---N hydrogen bond[53]. Whether this hydrogen bond will or will not survive in the protein pocket is an interesting question. But already it is clear that the porphyrin is an internal base that may participate in deprotonation/ protonation events.

3.7. Protonation of Cpd 0 and Formation of Cpd I (7)

DFT calculations show that ferric peroxide, Cpd 0 (**6**), is a fairly strong base with a high proton affinity; PA = 334 kcal mol^{-1} at BPW91 and with CH_3S^{-} proximal ligand[26] or 330.1 kcal mol^{-1} at B3LYP and with HS^{-} as the proximal ligand[40, 53]. Both studies found that the protonated species yields Cpd I (**7**) spontaneously without a barrier. In any event, the study of Davydov *et al.*[9] shows that mutation that replaces Thr_{252} does not prevent the formation of Cpd 0, but prevents, or at least slows down, its subsequent protonation to yield Cpd I. This suggests that the protonation mechanisms that lead to **5** and **6** are different. The protonation mechanism is thought to occur from a hydronium ion sequestered in $P450_{cam}$ by Asp_{251} and Thr_{252}

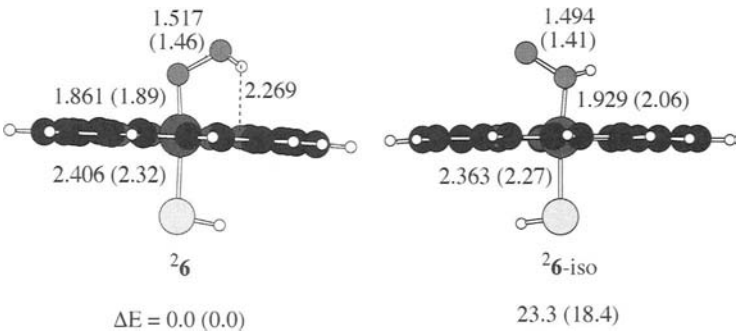

Figure 2.9. Optimized geometries of Cpd 0 (^{2}**6**) and its isomer ^{2}**6**-iso. Values out of parentheses are from Ogliaro *et al.*[53], values in parentheses are from Harris and Loew[26].

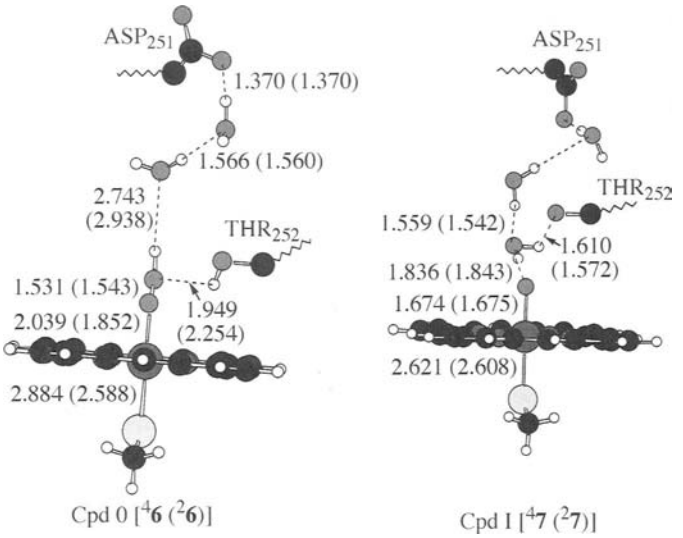

Figure 2.10. Hydrogen bonding set-up for protonation of Cpd 0 to Cpd I, from Kamachi and Yoshizawa[49].

(ref. [52]). A recent study of Kamachi and Yoshizawa[49] used a similar model to the one proposed by Vidakovic *et al.*[52] with two water molecules sequestered between the carboxylate end, CO_2^-, of Asp_{251} and the hydroxyl side chain of Thr_{252}, as shown in Figure 2.10. The protonation starts with a proton transfer from Thr_{252} to the distal oxygen of **6**, followed by a departure of a water molecule that is trapped through hydrogen bonding to the Thr_{252} anion and the array of the two waters that are linked by hydrogen bonding to the Asp_{251} anion. This mechanism predicts that the protonation of **6** and formation of **7** is exothermic by 13.1 and 5.5 kcal mol^{-1} for the quartet and doublet states, respectively. The entire protonation process from ^{2,4}**5** to ^{2,4}**7** by this Asp_{251}-Thr_{252} machinery was calculated to be exothermic by 74.6 (55.6) kcal mol^{-1} (ref. [49]). However, the barrier was not calculated for this process. Alternatively, the protonation mechanism may be nascent from a hydrogen-bonding array similar to the one discussed by Guallar *et al.*[48] and Harris[51]. This, to the best of our knowledge, has not been addressed by Harris[51].

In principle, protonation of Cpd 0, **6**, can occur on either the proximal or the distal oxygen of the complex. Distal protonation results in the departure of a water molecule and generation of Cpd I. Alternatively, proximal protonation gives a hydrogen peroxide complex. The latter complex is able to release H_2O_2 and return to the resting state by coordination with a water molecule, thereby leading to decoupling. Energetically, the formation of the hydrogen peroxide complex from **6** is only 6 kcal mol^{-1} less exothermic than that of Cpd I from **6** (ref. [26]), such that the decoupling reaction is a serious competitor with the productive process that leads to Cpd I. Not much is yet known about this competition. Clearly, a future theoretical study is required to explore alternative protonation pathways that can reveal the intricate behavior of the wild-type and mutant enzymes.

3.8. The "Push Effect" on the O–O Cleavage Process

The thiolate ligand was implicated as a crucial factor in the O–O bond cleavage process through its "push effect" that leads to Cpd I (ref. [54]). Ogliaro *et al.*[40] have addressed this issue by comparing the proton affinity of **6** to a reference complex without a thiolate ligand. The thiolate ligand was found to increase the proton affinity of ferric peroxide by 81 kcal mol^{-1}. At the same time, the protonated reference complex devoid of thiolate loses water spontaneously as well. Thus, the "push" effect of the thiolate does not concern

the mechanism of the O–O cleavage as such, if there could exist a strong enough acid to protonate the ferric peroxide devoid of a thiolate ligand. The "push" effect is expressed on the thermodynamics of the protonation, and by raising the proton affinity by 81 kcal mol^{-1}, the thiolate enables the protonation of **6** by moderate acids such as those that exist in the protein pocket. The roots of this "push" effect were analyzed and were found to consist of a combination of a field effect and an orbital effect[40]. The field effect originates in the electrostatic interaction of the negatively charged thiolate with the ferric peroxide moiety, while the orbital effect results from the mixing of the σ-hybrid of the thiolate with the a_{2u} orbital of the porphyrin (see Figure 2.3), which raises the energy of this orbital.

Another aspect of the "push" effect that was addressed by Ogliaro *et al.*[40] is the putative reduction of **6** by electron transfer. It was found that the reduction of **6** to $\mathbf{6}^-$ is highly endothermic by 43.3 kcal mol^{-1}, whereas in the absence of thiolate such a reduction would be exothermic by 35.1 kcal mol^{-1}. This very large change in the reduction energy is mostly due to the field effect of the negatively charged thiolate. This can be compared to the high proton affinity of **6**, which is very high due to the same "push" effect. Thus, the thiolate ligand endows ferric peroxide with selectivity to undergo protonation rather than accepting an additional electron.

3.9. Cpd I (7)

Initial DFT studies of Cpd I were done for the bare molecule, that is, in vacuum or gas phase conditions, and led to controversial results regarding the electronic structure of the ground state. These results showed sensitivity to the thiolate used to model the cysteinate ligand, as well as to the functional used to calculate the species. Nevertheless, all the calculations agreed that the species is a triradicaloid with three singly occupied orbitals. Two of these are the π^*_{xz} and π^*_{yz} orbitals, depicted above in Figure 2.3, which appear in all calculations including the CASSCF study of Cpd II[55]. However, the various studies differ significantly in the description of the third orbital, depending on the manner in which the study models the thiolate proximal ligand[16, 26, 35, 56–61]. The studies, especially those using mercaptide[60] or cysteinate anion devoid of its internal hydrogen bonding[61] predicted that the third singly occupied orbital is the p_π lone pair orbital on sulfur leading to $^{4,2}\Pi_S$ ($\pi^{*1}_{xz}\ \pi^{*1}_{yz}\ \pi^1_S$) states (Figure 2.3) with spin density almost exclusively on the sulfur while the porphyrin is closed shell. Other studies[57, 58] that used HS^- or cysteinate with its internal hydrogen-bonding interactions, found that the third singly occupied orbital is a_{2u} strongly mixed with the sulfur σ-hybrid (see Figure 2.3); this occupancy leads to $^{4,2}A_{2u}$ states, with spin density distributed over the porphyrin and sulfur. It was found[57, 62], that with HS^- or cysteinate as ligands, the $^{4,2}\Pi_S$ electronic states are more than 5 kcal mol^{-1} higher in energy than the $^{4,2}A_{2u}$ state, whereas with mercaptide all the four states were condensed to within 1 kcal mol^{-1}. This difference is not only academic but also has clear physical manifestations. Had Cpd I been a $^2\Pi_S$ ground state, it would have been red, as the Cpd II species with closed shell porphyrin, while if the ground state had been $^{4,2}A_{2u}$ type, the compound would have been green.

These considerations and other findings, which showed that the nature of the state is highly dependent on the Fe–S bond length[62], prompted a DFT study of the effect of the NH---S hydrogen bonding and the protein electric field on the nature of Cpd I, using simple modeling of these effects[58, 63]. Figure 2.11 depicts a typical result, by comparing the key bond lengths and spin densities (ρ) for the bare molecule, the molecule in an electric field characterized by a dielectric constant, ε = 5.7, and when the bare molecule is coordinated to two ammonia molecules by NH---S hydrogen bonds. As can be seen, under all conditions, the FeO moiety has two spins, while the third spin is distributed over the sulfur and porphyrin ligands in proportions that are highly dependent on the conditions. In the bare molecule, the third electron resides more on the sulfur than on the porphyrin, for example, ρ(Por) = 44% in the $^4A_{2u}$ state. With just two NH---S hydrogen bonds, the unpaired electron shifts mostly to the porphyrin, and so is the situation in a polarizing electric field (mimicked by a dielectric constant, ε = 5.7). Another interesting feature of Cpd I is that whereas most bond lengths do not change significantly with the application of hydrogen bonding and polarity, the Fe–S linkage gets shorter by almost 0.1 Å and its bond

dissociation energy increases significantly. These results led to the conclusion that Cpd I is a *chameleon species* that can change its character and electronic state in response to the environment to which it must accommodate[58, 63].

Recent QM(DFT)/MM calculations of Cpd I of $P450_{cam}$ (ref. [19]) used B3LYP, a variety of basis sets, three different thiolate ligand models, and four different snapshots selected from the MD trajectory after equilibration had been established (200 ps simulation). These calculations retrieved the important NH---S hydrogen bonds, donated to the sulfur by Leu_{358}, Gly_{359}, and Gln_{360}, and assigned Cpd I in a definitive manner as the doublet $^2A_{2u}$ state with a very closely lying $^4A_{2u}$ state; the same QM/MM description applies to the Cpd I irrespective of whether the proximal ligand was HS^-, CH_3S^- or a more extensive chunk of the cysteine loop. Thus, in accord with experimental results on the analogous Cpd I species of the enzyme chloroperoxidase[64], Cpd I of P450cam is a doublet state and it corresponds to the "green species."

The QM/MM calculations also confirmed the chameleonic nature of Cpd I, as can be gleaned from Figure 2.11. Thus, in the gas phase situation, the Fe–S bond was long and the third spin was located mostly on the sulfur, whereas in the protein environment, the Fe–S underwent shortening and the spin transferred to the porphyrin; in both respects, the gas phase situation with HS^- was closer to the QM/MM results[19] than

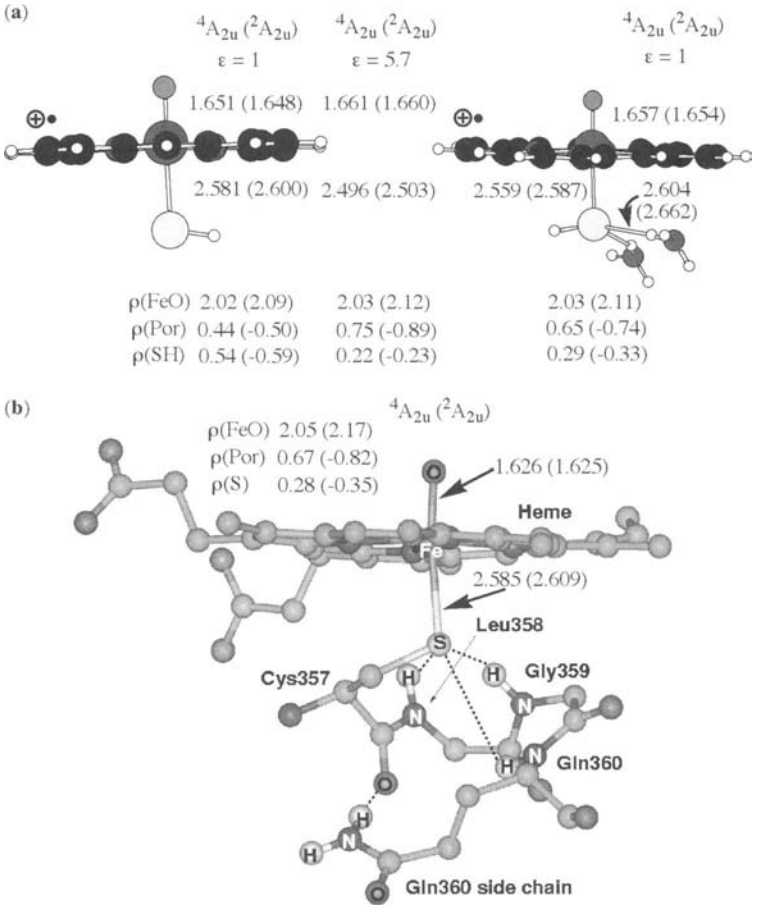

Figure 2.11. Hydrogen bonding (NH---S) and polarity effects (ε is the dielectric constant) on geometrical parameters and group spin densities (ρ) of Cpd I. (a) Model calculations[63]. (b) QM/MM calculations[19].

the more extensive proximal ligand model, for example, mercaptide or cysteinate anion. A very interesting feature of the QM/MM study[19] is the variation in sulfur/porphyrin spin densities and Fe–S bond length, imparted by the NH---O=C hydrogen bond, donated to the carbonyl group of the cysteine ligand by the side-chain Gln_{360}. As this hydrogen bond was allowed to intensify and change gradually toward its X-ray position, so did the porphyrin spin density increase, the sulfur's spin density decrease, and the Fe–S bond length gets shorter. Thus, fine-tuning the hydrogen-bonding interaction around the thiolate ligand fine-tunes the electronic structure of Cpd I and its Fe–S bond length; Cpd I is indeed a chameleon species that will be different for different P450 isozymes.

A simple valence bond (VB) model was used to account for this chameleon nature of Cpd I, as shown in Figure 2.12[19, 57, 63]. The electronic structure of Cpd I can be constructed from two resonance structures, |**a**> and |**b**>; |**a**> describes a thiolyl radical and a closed-shell iron-oxo porphyrin, while |**b**> is an ion pair composed of a thiolate anion and an iron-oxo porphyrin cation radical. In the gas phase and at infinite Fe–S distance, |**a**> is much lower than |**b**>. However, at the equilibrium distance in the gas phase, |**b**> gets stabilized by electrostatic interactions and closely approaches |**a**>, but is still above |**a**>. The mixing of the resonance structures will lead to a state that is |**a**>-like with a preponderant S• character. This character in the gas phase for the molecule will depend strongly on the donor capability of the thiolate ligand; it will be larger for a model like CH_3S^- and smaller for a model like HS^- that is a relatively poorer donor. In a polarizing electric field and in the presence of NH---S hydrogen bonds, the ion-pair structure |**b**> gets stabilized and descends below |**a**>; the mixed state is now |**b**>-like and has a $S:^-Por^{\bullet+}$ character. It is apparent that this model predicts that as the hydrogen-bonding situation and strength of the polarizing field increase so will the $Por^{\bullet+}$ character. It is also apparent from Figure 2.12(b) that by changing from S•-like to $S:^-$-like, the sulfur changes its Fe–S bonding from a weak one-electron bond to a strong two-electron bond. Thus, the VB model shows that Cpd I is a mixed-valent state and as

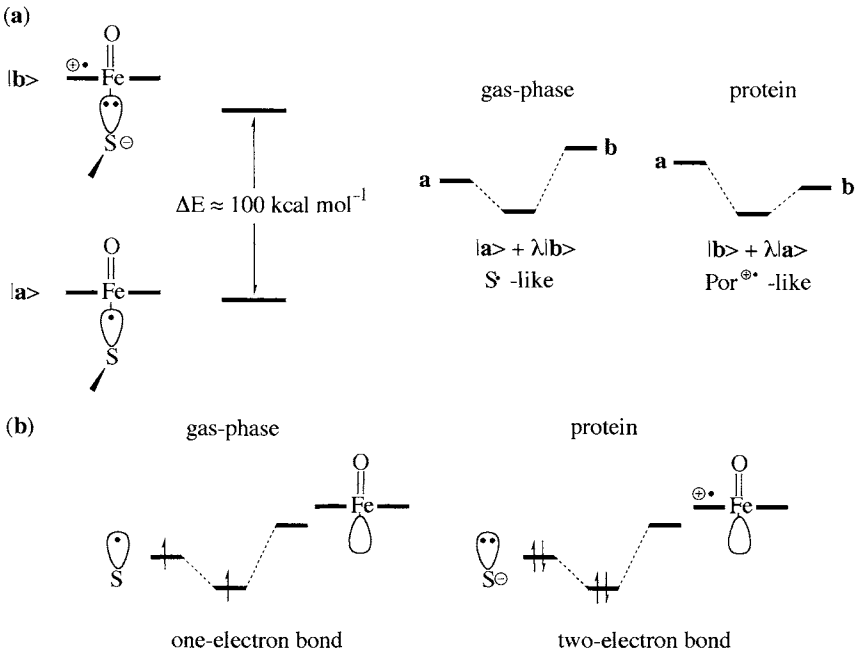

Figure 2.12. Modeling the influence of hydrogen bonding and polarity effects on the electronic structure of Cpd I: (a) Valence bond mixing of the contributing structures. (b) The Fe–S bond orbital, its occupancy and the type of the Fe–S bond.

such will change its electronic structure and Fe–S bond length depending on the hydrogen-bonding machinery and the electric field of the protein pocket that accommodates it; it will behave as *a chemical chameleon*.

Many other Cpd I species for different enzymes and model systems were studied, and it is worthwhile to mention some of these even if they are not P450 species. Ohta *et al.*[61] performed DFT-B3LYP calculations with a methoxide axial ligand and found a LS ground state ($^2A_{2u}$) that contained 64–69% unpaired spin density on the axial ligand and 22–33% on the porphyrin ring. It is most likely that being a good electron donor, methoxide will endow its Cpd I with a *chameleonic behavior*, which has not yet been studied. DFT calculations with the iron substituted by manganese[65] or by ruthenium[66] showed that these systems have different ground states than Cpd I of P450, and therefore will show differences in reactivity as shown subsequently by Sharma *et al.*[67]. These differences do not arise from changes in the nature of the orbitals, shown above in Figure 2.3, but rather from the relative energy of the orbitals being modulated by the transition metal. In particular, in the ruthenium substituted Cpd I species with HS^- as a proximal ligand, the ground state involves Ru^V with a single unpaired electron in the π^*_{xz} orbital labeled $^2\Pi_{xz}(Ru^V)$[66]. This state was found to be 4.58 kcal mol^{-1} lower lying than the $^2A_{2u}$ state. In contrast, in the case of Cpd I with iron, the $^2\Pi_{xz}(Fe^V)$ state was found to be 22 kcal mol^{-1} higher in energy than the $^2A_{2u}$ ground state. However, in the case of Cpd I (Ru) too, the $^{4,2}A_{2u}$ states exhibit a chameleonic behavior, and become the ground states when medium polarity effect is taken into account. Thus, the Cpd I(Ru) species offers a wonderful opportunity to tune the nature and identity of the ground state and possibly also the reactivity patterns, by changing the proximal ligand, by substituting the porphyrin, and by changing the polarity of the medium[66, 67].

Replacing the cysteinate axial ligand with either imidazole[68] or phenolate[69] models the related enzymes HRP and catalase, respectively. In contrast to cysteinate, an imidazole ligand hardly interacts with the porphyrin a_{2u} orbital. As a result, the spin densities of the singly occupied a_{2u} orbital in Cpd I(HRP) are primarily located on the porphyrin ring, while in Cpd I(P450), the spin density is spread over the porphyrin and cysteinate groups. Kuramochi *et al.*[12] found an energy gap of 0.15 eV (3.46 kcal mol^{-1}) between the ground state $^4A_{2u}$ and the excited $^4A_{1u}$ states of a HRP model Cpd I with imidazole as the axial ligand. Subsequently, Deeth[70] studied the same species and showed that the most stable isomer involves saddling of the porphyrin that stabilizes the molecule by 2.5 kcal mol^{-1}. No saddling was observed for thiolate ligands with porphine or octamethyl porphyrin[58]. However, with *meso*-tetramethylporphyrin, a significant saddling was observed[71] even when the proximal ligand was thiolate. The saddling of the *meso*-tetra-substituted-porphyrinated Cpd I species was interpreted as the means to relieve the steric repulsion between the *meso* substituent and the hydrogen substituents on the α and β positions[71].

The influence of the neighboring amino acids on the stability of Cpd I for HRP was studied by Wirstam *et al.*[72] using DFT calculations. Their model used oxo-iron porphyrin and an imidazole ligand replacing His_{175}, a formate anion replacing Asp_{235} and an indole group instead of Trp_{191}; all these three amino acids are located on the proximal side of the porphyrin. In their optimized, geometry, the indole moiety (of Trp_{191}) is protonated and the formate group (of Asp_{235}) is negatively charged forming hydrogen bonds with both the imidazole and the indole groups. It was found that in the HS state (S = 3/2), two spins are located on the FeO unit, while the third one is shared between the porphyrin and indole groups 0.48 and 0.47, respectively. Once again, it is apparent that the porphyrin cation radical is eager to share its hole with other good donors. Perhaps the chameleon behavior is general for Cpd I species, even when the proximal ligand itself cannot participate in electron donation to the "hole," other, better donor moieties will take its role.

Green[69] calculated the low-lying electronic states of Cpd I for a catalase model, with phenolate as the proximal ligand. He found that the ground state had the LS $\pi^{*1}_{xz}\ \pi^{*1}_{yz}\ \pi_L{}^1$ configuration, with π_L being a lone-pair orbital on the phenoxy ligand. Two spins were located on the FeO moiety and the third almost exclusively on the phenoxy ligand. A hydrogen bond donating to the oxygen of the phenolate ligand, or the placement of cationic species that mimic the presence of a charge-relay system in the protein, caused

a significant change and shifted half of the spin density from the phenoxy ligand to the porphyrin[69]. These results are similar to the ones obtained for Cpd I of P450[19, 58, 63] and indicate that the *chameleon* concept may well be a general paradigm for heme enzymes.

3.10. What Makes the Catalytic Cycle Tick? A Summary

Two factors, mentioned above, emerge from the calculations to strongly influence the catalytic cycle: one is the "push" effect of the thiolate and the other is the hydrogen-bonding machinery that is involved in protonation mechanisms of **5** and **6** as well as in stabilization of Cpd I. The "push" effect is associated with the strong electron donor property of the thiolate ligand. The calculations of Ogliaro *et al.*[40] showed that the "push" effect is responsible for gating the cycle by a single molecule of water; for the O–O cleavage; for the preference of the twice-reduced species **5** and the ferric peroxide Cpd 0 species, **6**, to undergo protonation rather than reduction; and for the propensity of Cpd I to participate in hydrogen abstraction or bond-making processes over electron transfer process. Without the thiolate ligand or with one that is a much lesser electron donor than thiolate, the resting state, as well as **5** and **6**, would have been prone to reduction, the O–O bond cleavage process would have been highly endothermic, and Cpd I would have been an extremely powerful electron acceptor. Thus, the thiolate creates selectivity toward reduction and thereby contributes to a stable cycle with a tightly gated reducibility and basicity of the various species.

The calculations of Guallar *et al.*[48] and of Harris[51] demonstrate that the hydrogen-bonding machinery provides the means for a gentle protonation that can protonate the twice-reduced species, **5**, without touching its precursor ferrous-dioxygen complex, **4**. This gentle machinery awaits, therefore, patiently the second electron transfer and, hence, ultimately enables the generation of Cpd I. The study of Kamachi and Yoshizawa[49] offers an alternative protonation mechanism that is more potent and exothermic than the one advocated by Harris[51], and which applies to both the doublet and the quartet states of **5**. This mechanism is based on a proposal of Vidakovic *et al.*[52] and involves the acidic CO_2H proton of Asp_{251} that is transferred via an array of two waters. Protonation of ferric peroxide species, **6**, appears, however, to proceed by a gentler machinery[49] with exothermicity of *c.*13.1 and 5.5 kcal mol^{-1} (Figure 2.10), respectively, for the quartet and the doublet states. These multiple protonation pathways suggest very strongly that both the doublet and the quartet states of Cpd I may be formed separately, and those mutations may affect the production of the two states in a different manner.

4. MM and MM/MD Studies of P450 Reactivity Aspects

This section reviews MM/MD theoretical work, which addresses the entrance of the substrate to the pocket, its binding, and the exit of the substrate. Much theoretical work that rely on quantitative structure activity relations, QSAR, is not reviewed, but can be found in the authoritative treatment of Lewis[73].

4.1. Studies of Substrate Entrance, Binding, and Product Exit

P450 enzymes usually have an active-site pocket that is equipped with a substrate binding and O=O cleavage machineries[74, 75]. Figure 2.13 shows the QM/MM calculated camphor within the pocket of $P450_{cam}$, in the presence of Cpd I[76]. In accord with experiment, the calculations reveal that two amino acids participate in the substrate binding; Tyr_{96} holds camphor by an OH---O=C hydrogen bond and Val_{295} interacts with the bridge methyl groups of camphor and thereby sequesters the substrate. Other P450 isozymes have their own specific machineries and still others have larger and less selective pockets. Substrate access to the pocket, binding, and product exit have been probed by a variety of experimental techniques, and have been theoretically studied by means of docking and MM/MD simulation techniques of various types.

Docking calculations followed by MM/MD and Monte Carlo simulations on the catalytic metabolism of the insecticide carbofuran by

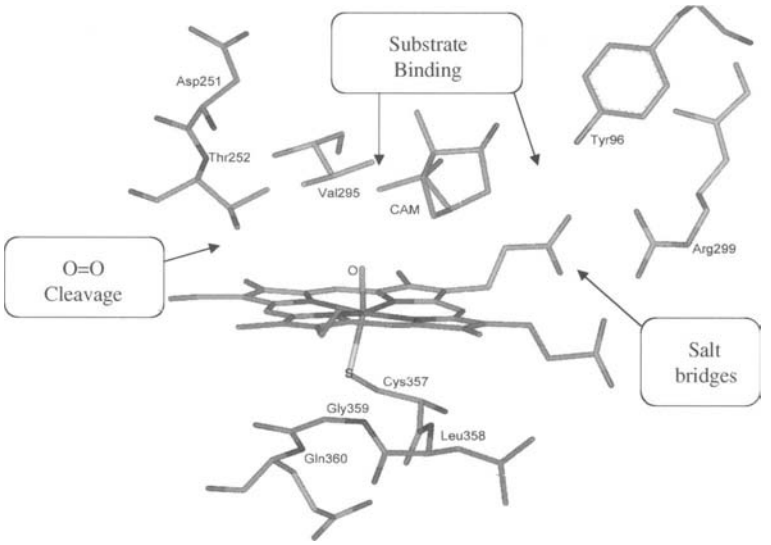

Figure 2.13. The active site of $P450_{cam}$ showing functions of various residues.

$P450_{cam}$ were performed by Keserü *et al.*[77] and Keserü *et al.*[78]; the tight binding of carbofuran by hydrogen bonding to Tyr_{96} and its steric confinement by Val_{247} and Val_{295} were found to fit the preferred regioselectivity and stereospecificity of hydroxylation at the C3 atom of carbofuran. Cavalli and Recanatini[79] used docking simulations to study the selectivity of P450 inhibitors that carry imidazole groups, and found that the inhibitors bind to the heme via the lone pair of nitrogen in the imidazole group. This theoretical approach, and similar ones not reviewed here, tacitly assumes that the preferred position of the substrate *vis-à-vis* the active species can foretell the regio- and stereospecificity of the monooxygenation process, as well as efficacy patterns of inhibitors.

Other approaches, which combined experimental and theoretical studies, revealed some generalities on binding modes and motions within the pocket. NMR results[80] of perdeuterated adamantane in $P450_{cam}$ indicate that the substrate is conformationally mobile on the timescale of the enzymatic turnover. This mobility was further revealed by docking studies[81] of various substrates and inhibitors of $P450_{cam}$. It was found that the general strategy of rigid docking, which seeks substrates that fill the active site completely, fails to reproduce their set of experimental data about the enzyme function. A successful strategy was found to require, *inter alia*, active site plasticity and considerable movement of the substrate, which thereby enable substrate positioning and catalytic function. Other studies revealed that some of the substrate motions are more constrained than others and depend on the topography of the pocket and the substrate. Thus, the experimental results of Atkins and Sligar[82] show that during camphor hydroxylation by $P450_{cam}$ the hydrogen is initially abstracted from both *exo* and *endo* C–H bonds, but the process only produces the *exo* alcohol product. This result indicates that after the hydrogen abstraction, the alcohol formation step is sufficiently fast to reveal the restriction of the camphor by its binding in the pocket. Similarly, MD simulations and experimental studies[83] of the kinetic isotope effect (KIE), for hydroxylation of xylenes and 4,4′-dimethylbiphenyl, having equivalent, but isotopically distinct, methyl and deuterated methyl groups indicated that the mode that switches the position of the two methyl groups is restricted in proportion to the distance between the groups. This restriction masks the intramolecular KIE value for 4,4′-dimethylbiphenyl for which the distance is 11.05 Å, and the KIE drops from *c.*7–10

to *c*.2.7. In summary, the above studies show that the outcome of a given experiment depends on the interplay of the rate constants for substrate binding, de-binding, monooxygenation, and tumbling. Being "free" or "restricted" has a relative meaning depending on the timescale of the various processes.

Still other approaches use MM/MD simulation to study the dynamics of various processes associated with the water content of the protein pocket and the entrance and exit of substrates therefrom. The hydration of the protein cavity was studied by Helms and Wade[84] using MD simulations of the substrate-free $P450_{cam}$ followed by thermodynamic integration. It was found that although the cavity could hold, in principle, 10 water molecules, the thermodynamically most favorable water content in the pocket was 6 molecules; most of them occupied the site of the sixth axial ligand (distal ligand) and one was coordinated to Tyr_{96}. The water molecules in the pocket were spread over a larger volume than in bulk water, and were therefore more mobile than bulk water molecules. MD simulations of the substrate entrance and exit channels of $P450_{cam}$, $P450_{BM-3}$, and $P450_{eryF}$ were studied by Lüdemann *et al.*[5, 6] and Winn *et al.*[85]. In all cases, the major access channels were found to coincide with the ones predicted from crystallographic data based on thermal fluctuation factors (B factors) near the F/G loop and adjacent helices. All these mechanisms involve backbone motions and rotations that are specifically tailored to the physico-chemical properties of the substrate. In $P450_{cam}$, the channel is typified by small backbone displacements (1.8–2.4 Å) and aromatic side-chain rotations of Phe_{87}, Phe_{193}, and Tyr_{29}. In $P450_{BM-3}$, the positively charged Arg_{47} located in the entrance of the channel makes a salt-link that guides the negatively charged substrate via its carboxylate group, while in $P450_{eryF}$, the Arg_{185} residue rotates and, by making intraprotein hydrogen bonds, gates the channel opening. Will such entrance/exit studies eventually account for the specificity of the P450 isozymes, as hoped by the MM modeling community? It is a question that merits a proof of principle. Should this turn out to be the right approach to the problem, then all the chemical details of P450 activation would be immaterial to its action. As shown below, this is certainly not the case.

4.2. MM and MM/MD Studies of Regioselectivity

An MD simulation technique was applied by Audergon *et al.*[83] to analyze the regio- and stereoselectivities of hydroxylation of the (1*R*)- and (1*S*)-norcamphor by $P450_{cam}$. X-ray structures of the substrate–enzyme complex for the two enantiomers of camphor showed that (1*R*) is oriented with its C5 atom pointing toward the heme iron, whereas (1*S*) exhibits significant disorder. Despite the different substrate-binding conformations of the two enantiomers, both are known to give exclusively *exo*-C5-hydroxylation. To resolve this apparent inconsistency between the two sets of experimental results, Das *et al.*[86] performed MD simulation on the substrate binding of these two camphor enantiomers to $P450_{cam}$. The results[86] for both enantiomers revealed the strong orienting effect of the hydrogen bond to Tyr_{96}. However, while the (1*R*) enantiomer gave one stable structure, the (1*S*) enantiomer had greater mobility in the active-site pocket. In addition, the (1*R*) enantiomer was found to orient with its C5 atom pointing toward the heme iron, whereas this was not the case for the (1*S*) enantiomer. These differences accounted for the X-ray structural findings. To address the apparent inconsistency between the experimental X-ray and reactivity data, the simulation was repeated with a water molecule as the sixth ligand. The presence of the water molecule was found to reorient the (1*S*) enantiomer with a C5 contact to the heme. This result was interpreted by the authors as a resolution of the inconsistency, based on the contention that regioselectivity ultimately depends on the orientation of the substrate *vis-à-vis* the ferryl oxygen of Cpd I. The same technique was employed for the monooxygenation of styrene by $P450_{cam}$ (ref. [87]) where a good fit was obtained between product distribution and the docked conformation.

MD simulation studies by Harris and Loew[88] were used to rationalize the regiospecificity of hydroxylation of camphor and a variety of other substrates. A series of trajectory calculations were performed for the enzyme–substrate interactions, and these results were coupled with relative stability of the organic radical intermediates to predict the product distributions. In a recent paper, Park and Harris[89] employed an integrated

modeling approach that involves comparative modeling (sequence and SCR alignment), a *de novo* loop construction and MD equilibration, to reconstruct a model of $P450_{2E1}$ of sufficient accuracy to ascertain the geometric determinants of diverse substrate metabolism via configurational sampling techniques. Energy-based docking was shown to be an adequate predictor of binding modes correlated with experimentally deduced metabolites. An MD-configurational sampling based on the low-energy docked configurations was found to be a more accurate predictor of geometric factors. In this manner, it was possible to screen many substrates and locate the lowest energy enzyme–substrate complexes. Assessment of the relative hydroxylation efficiency of three prototypical substrates at their various functional groups was carried out by combination of MD sampling, of the docked configurations, and an energy criterion of the relative DFT-calculated energies of the radical intermediates produced in the reaction by hydrogen abstraction (see mechanisms below). The relative energies of the radicals were found to be good predictors of the relative barriers of the C–H abstraction step. In several instances, these workers found that while equivalent geometric exposure of metabolical sites occurred, *an accurate prediction of the metabolite pattern could be made only by means of electronic and energetic factors deduced from DFT.*

In summary, investigations of P450 mechanistic problems by reliance on the modes of substrate entrance and binding as the determinants of all the subsequent chemistry, while being a tempting and an economical approach to the problem, are, in our view, not well founded. Importantly, such approaches miss the crucial factors concerning the electronic structure determinants of the processes, as discussed in the rest of the review. The recent results of Park and Harris[89] support this conclusion and highlight the crucial nature of the fundamental mechanistic investigations by means of QM calculation, as reviewed in the remainder of this chapter.

5. QM Studies of P450 Reactivity Patterns

Cpd I is considered to be the primary reactive species of P450 enzymes. However, Cpd 0 (**6**) has been implicated as a second oxidant that functions alongside Cpd I, or in its absence, for example, in mutant enzymes where the O–O cleavage machinery has been impaired[90, 91]. Recent results on the mutant enzyme of $P450_{cam}$ (ref. [92]) show that the mutant $P450_{cam}$ (T252A), where the threonine that is responsible for the efficient protonation machinery is mutated to an alanine, does not hydroxylate camphor, but does epoxidize camphene, albeit much less efficient than in the wild-type enzyme. It was postulated that, in the absence of Cpd I, Cpd 0 was the likely oxidant but that it is a much less efficient oxidizing species than Cpd I. The next few sections outline the results of QM and QM/MM calculations on some of the major reactions of P450: alkane hydroxylation, alkene epoxidation, benzene hydroxylation, and sulfoxidation. These reactions were studied using Cpd I as the electrophilic oxidant. Two reactions, ethene epoxidation and sulfoxidation, were studied with both Cpd I and Cpd 0.

5.1. Reactivity of Cpd I: General Considerations of the Origins of Two-State Reactivity (TSR) of Cpd I

As seen already, Cpd I is a triradicaloid with singly occupied π^*_{xz}, π^*_{yz} and a_{2u} orbitals and, hence, has a virtually degenerate pair of ground states ($^{4,2}A_{2u}$). As such, it is expected that at least these electronic states will participate in the reactions, and will lead thereby to two-state reactivity (TSR)[93–95]. In TSR, each state may produce its specific set of products with different rate-constants, regio- and stereoselectivities and lead thereby to apparently controversial information when viewed through the perspective of single-state reactivity (SSR). It is our contention that TSR resolves much of the controversy that has typified the P450 field of reaction mechanism in recent years[95], and opens new horizons for reactivity studies.

5.2. A Primer to P450 Reactivity: Counting of Electrons

As a prelude to the reactivity discussion, it is worthwhile to appreciate an important generalization, namely that the synchronous oxene insertion

by Cpd I is a forbidden reaction[96, 97], and that we expect, therefore, to deal with essentially nonsynchronous processes even if some of the mechanisms may turn out to be effectively concerted. To assist us in keeping track of the electron count during this formal "two-electron oxidation" process, we present in Figure 2.14, an oxidation state-orbital occupancy diagram that follows the electronic reorganization and accounts for the formal oxidation states of Cpd I and the substrate at various phases of the process. The substrate is chosen to be one that can undergo hydroxylation or epoxidation and is symbolized by its two main active orbitals, the σ_{CH} orbital that figures in hydroxylation and π_{CC} that is important for epoxidation. Thus, initially Cpd I involves Fe^{IV} and porphyrin radical cation ($Por^{+\bullet}$), that is, the effective oxidation state is Fe^{V}. As Cpd I and the substrate make one bond (O–H or O–C), a single electron shifts from the appropriate orbital of the substrate (σ_{CH} or π_{CC}) to either the a_{2u} orbital of the porphyrin (**1**), or to the π^*_{xz} orbital of the FeO moiety (**2**), leaving a singly occupied orbital labeled as ϕ_C on the substrate. Now, the effective oxidation state of the heme species is reduced to Fe^{IV} (either $Fe^{III}Por^{+\bullet}$ or $Fe^{IV}Por$) accounting for

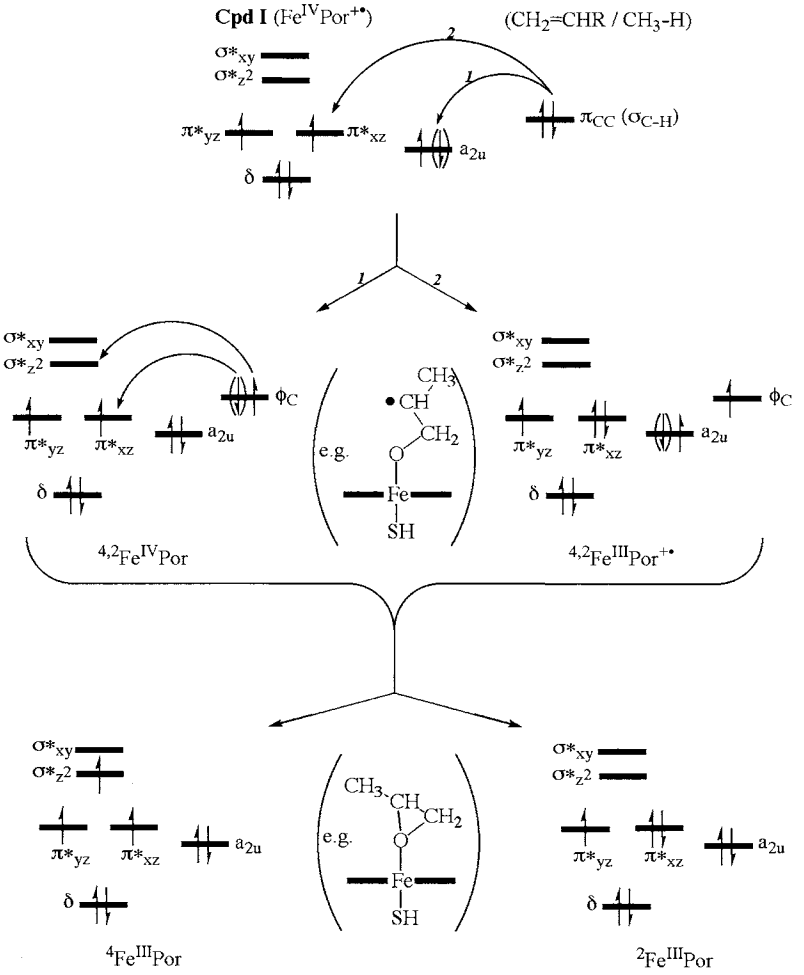

Figure 2.14. Oxidation-states and orbital occupancy diagrams in various stages of alkene epoxidation and alkane hydroxylation. Occupations within parentheses show the alternative spin arrangement, of the odd electron, in the corresponding low-spin state.

the first oxidation equivalent. In the second phase, the substrate forms a second bond with the oxo group of the heme, and a second electron is shifted from the singly occupied substrate orbital ϕ_C to the heme to populate either the $\sigma^*_{z^2}$ orbital, which results in a quartet state of the product complex, or to the π^*_{xz} orbital of $Fe^{IV}Por$ or the a_{2u} orbital of $Fe^{III}Por^{+\bullet}$; the latter two options give the doublet state of the product complex. The last step accounts for the second oxidation equivalent, and the effective oxidation state of the heme is further reduced to Fe^{III}.

5.3. Alkane Hydroxylation

The mechanism of alkane hydroxylation is called the "rebound" mechanism. It transpires via an initial hydrogen abstraction, followed by rebound of the alkyl radical onto the oxygen of the iron-hydroxo species, Figure 2.15(a)[98]. This mechanism accounts for two key observations: (a) a small but detectable amount of stereochemical scrambling, and (b) a large KIE due to replacement of the hydrogen by deuterium in the C–H bond undergoing hydroxylation. The first measurement of radical lifetime by Ortiz de Montellano and Stearns[99] indicated that the radical derived from bicyclo[2.1.0]pentane had a finite, albeit short, lifetime. Everything looked fine for the rebound mechanism until Newcomb *et al.*[91, 100] used their ultrafast radical clocks to determine radical lifetimes. Figure 2.15(b) depicts a typical probe substrate used by Newcomb and its rearrangement pattern; the corresponding lifetime is determined from the inverse of the rate constant (k_R) of radical rearrangement and the ratio [***R/U***] of rearranged to unrearranged alcohol products. Using this method and determining only those [***R/U***] quantities that do not involve carbocation rearrangement, the resulting lifetimes quantified by Newcomb were in the order of 80–200 fs (ref. [100]). Since these lifetimes are too short to correspond to a real intermediate, Newcomb concluded that radicals are not present during the reaction and questioned the validity of the rebound mechanism.

This problem was taken on by the Jerusalem group who used DFT (B3LYP) computations to model the mechanism of methane hydroxylation[62, 101–103], allylic hydroxylation of propene[104, 105], and recently also of camphor hydroxylation by QM and QM/MM calculations[76]. In all these cases, we could not locate a TS for a concerted oxene insertion because the process possesses barriers that

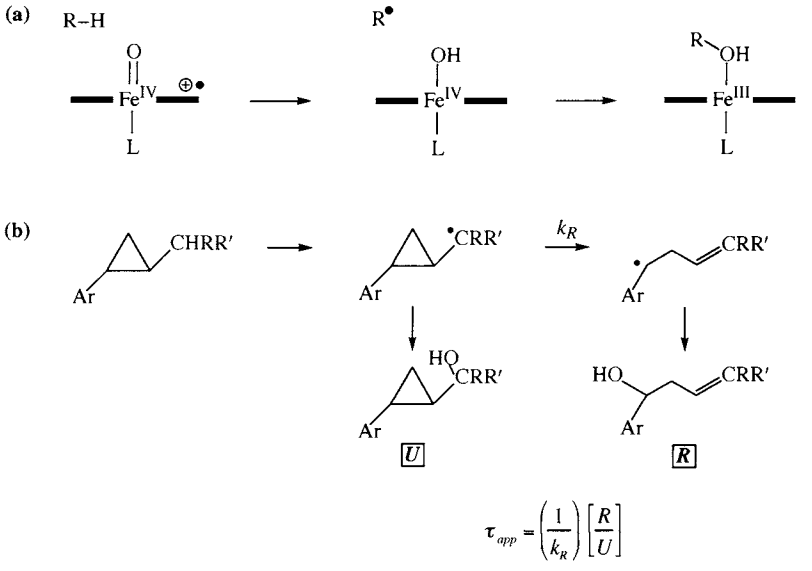

Figure 2.15. (a) The rebound mechanism. (b) Derivation of the apparent lifetime (τ_{app}) of a putative radical intermediate from the ratio of rearranged (***R***) to unrearranged (***U***) alcohol products produced from P450 hydroxylation of a substrate probe.

are too high and transition structures that are not real TSs; for example, they are second-order saddle points. The lowest energy mechanism was found to involve a hydrogen-abstraction like TS (TS_H), as exemplified in Figure 2.16 for camphor hydroxylation[76, 106]. However, the calculations reveal, as conjectured above, that the mechanism involves TSR nascent from the degenerate ground state of Cpd I that was modeled by the simplest system (with a porphine macrocycle and HS^- as a proximal ligand). Subsequent studies of ethane and camphor hydroxylation by the Yoshizawa group[49, 107–111] and of methane hydroxylation by Hata *et al.*[112], used porphine macrocycle and CH_3S^- as a proximal ligand, and arrived at basically the same conclusion, that the mechanism is typified by TSR.

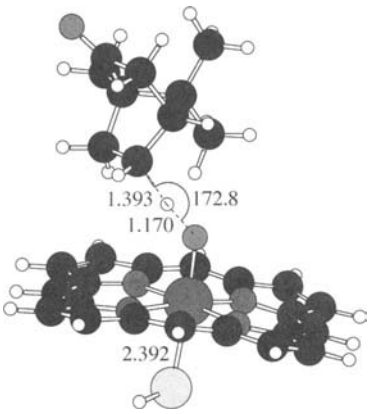

Figure 2.16. Camphor hydroxylation high-spin TS.

A typical reaction mechanism is shown in Figure 2.17, where one can see the doubling of the profile due to the HS and LS states. The reaction pathway involves three phases: (a) a C–H abstraction phase that leads to an alkyl radical coordinated to the iron-hydroxo complex by a weak OH---C hydrogen bond, labeled as $^{4,2}C_I$. (b) an alkyl (or OH) rotation phase whereby the alkyl group achieves a favorable orientation for rebound, and (c) a rebound phase that leads to C–O bond making and the ferric-alcohol complexes, $^{4,2}P$. The two profiles remain close in energy throughout the first two phases and then bifurcate. Whereas the HS state exhibits a significant barrier and a genuine TS for rebound, in the LS state, once the right orientation of the alkyl group is achieved, the LS rebound proceeds in a virtually barrier-free fashion to the alcohol. As such, alkane hydroxylation proceeds by TSR, in which the HS mechanism is truly stepwise with a finite lifetime for the radical intermediate, whereas the LS mechanism is effectively concerted with an ultrashort lifetime for the radical intermediate. A recent study of camphor hydroxylation[49] identifies a rebound TS for the LS process; this TS has a barrier of 0.7 kcal mol^{-1} but is merely the rotational barrier of the camphor to the rebound position.

By referring to Figures 2.15(b) and 2.17, it is possible to rationalize the clock data of Newcomb in a simple manner. The apparent lifetimes are determined from the rate constant of free radical rearrangement and the ratio [***R/U***] of rearranged to unrearranged alcohol product, assuming a

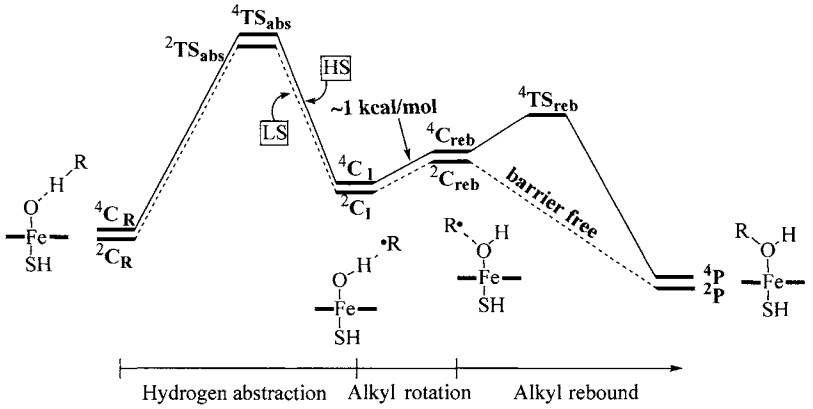

Figure 2.17. A two-state reactivity potential energy surface for alkane (R–H) hydroxylation by Cpd I.

single-state reactivity (SSR). However, in TSR, the rearranged product, ***R***, is formed only on the HS surface, while the unrearranged product, ***U***, is formed on the LS and possibly also on the HS surface. Therefore, the ratio, [***R/U***], is associated with the relative yields of the HS *vis-à-vis* the LS reactions and not with the radical lifetime as such[62, 95]. A simple TSR scheme leads to the following expression for the ratio of the real to the apparent lifetimes:

$$\tau_{REAL}(\mathrm{TSR})/\tau_{APP} = \frac{\{[\boldsymbol{U/R}]\,(1+F)\}}{\{[\boldsymbol{U/R}]-F\}} > 1, \qquad F = [\boldsymbol{LS/HS}], \quad (1)$$

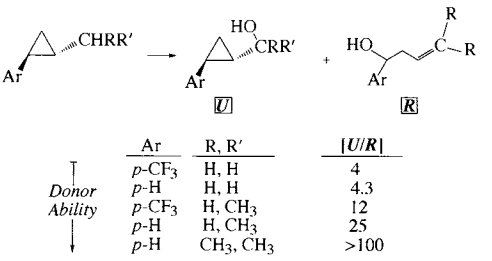

Figure 2.18. Experimentally determined ratios of unrearranged to rearranged product of various probes. The probes are arranged from top to bottom in order of increasing donor ability.

where the quantity F is the relative yield of the LS to HS reactions. It is clear that the real lifetime of the radicals on the HS surface is longer than the apparent lifetime in proportion to the value of F, the LS *vis-à-vis* HS yield. Since in the calculations the LS bond activation barrier is lower than the corresponding HS barrier, the F is larger than unity[62]; in the case of allylic hydroxylation, it reaches values of the order of 10 when the effect of the protein electric field and hydrogen bonding are taken into account[104, 105]. As such, the apparent radical lifetimes will be unrealistically short compared with the real lifetimes. Furthermore, analysis of the rebound process itself[62, 95, 102] showed that the quantity [***U/R***] should increase significantly as the alkane and its derived radical become better electron donors. Therefore, in such a series, the [***U/R***] quantity gradually increases, such that at some critical donor ability of the radical when the HS rebound barrier altogether vanishes, the [***U/R***] quantity converges to infinity, and the apparent lifetime becomes strictly meaningless. Such a trend has been observed in the series of probe substrates (*trans*-alkylarylcyclopropanes) used by Newcomb *et al.*[100] where the substrate, which is the best donor and which leads to the best donor radical, exhibits virtually no rearrangement. This Newcomb series is shown in Figure 2.18, which arranges the substrates in the order of increasing donor ability and displays the corresponding [***U/R***] quantity that exceeds 100 for the best donor situation.

Calculations of Yoshizawa *et al.*[108–111] using CH_3S^- as a proximal ligand retrieved the TSR scenario, and recently also the rebound barrier behavior of the LS and HS states[49]. However, these calculations reverse the ordering of the bond activation $^{2,4}TS_H$ species from "LS-below-HS" as in Figure 2.17, to "HS-below-LS." In addition, the LS pathway involves Fe^{III}, whereas by contrast, the HS pathway is Fe^{IV} type. We think that this inversion of the HS–LS ordering originates in the powerful electron donor property of the CH_3S^- ligand, such that its gas phase calculations do not represent as well as the HS^- ligand the actual situation of the cysteinate within the protein pocket[19]. Thus, much the same as in the case of Cpd I where the use of CH_3S^- as a proximal ligand in a gas phase calculation leads to a wrong assignment of the ground state (as a $^2\Pi_S$ state), this ligand also misrepresents the LS–HS energy difference of the bond activation TS_H species. In fact, QM/MM calculations of camphor hydroxylation by $P450_{cam}$ (ref. [76]) lead to a TS-situation of LS below HS, in agreement with the model studies of Ogliaro *et al.*[62, 103] and De Visser *et al.*[104, 105] using HS^- as a proximal ligand.

Figure 2.19 displays bond activation $^{2,4}TS_H$ structures for methane, ethane, propene, and camphor hydroxylation. It is apparent that irrespective of the alkane and proximal ligand model, all the TSs exhibit an almost linear O---H---C triad of atoms. These species closely resemble the genuine hydrogen abstraction TSs by alkoxyl radicals, one of which is also displayed in the figure. The computed KIE (T = 300 K) values of the P450 TSs range between 5.1 and 10.5 for the various substrates and models[49, 103, 105, 110] and are in good agreement with experimental values[95, 103].

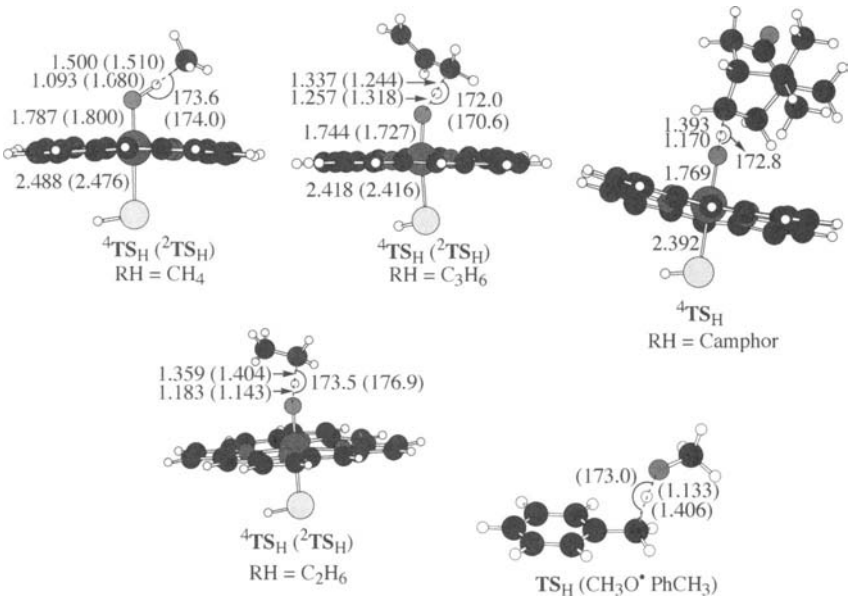

Figure 2.19. Hydrogen abstraction transition states (TSs) for some model reactions. The structures for methane and allylic hydroxylation are taken from Ogliaro *et al.*[62, 103] and De Visser *et al.*[105], the structure for H-abstraction from toluene from Ogliaro *et al.*[103], while for ethane hydroxylation from Yoshizawa *et al.*[111]. Key geometric parameters outside parentheses correspond to the high-spin TS, while those within to the corresponding low-spin structure.

The hydrogen abstraction barriers in alkane hydroxylation shown in Table 2.1 exhibit a high sensitivity to the donor property of the alkane and the C–H bond energy. They range from 26.7, 26.5 (HS, LS) kcal mol^{-1} for methane down to 13.5 kcal mol^{-1} for allylic hydroxylation. This trend was analyzed and shown to conform to hydrogen abstraction and oxidative character of the bond activation step, as outlined above in the oxidation state-orbital population diagram in Figure 2.14[62, 105]. Another feature in Table 2.1 is the reduction of the hydrogen abstraction barrier when zero point energy (ZPE) is included. This arises due to the loss of the ZPE for the C–H bond that is cleaved in the bond activation $^{2,4}TS_H$ species. Another feature in Table 2.1 is the very significant entropic contribution to the free-energy barrier. Much of this arises due to the loss of translational and rotational degrees of freedom and structural stiffening in the $^{2,4}TS_H$ species. Substrate binding within the enzyme is, to a large extent, entropically driven, because it causes expulsion of the water molecules from the binding pocket. Since the hydroxylation begins with the bound substrate,

Table 2.1. Hydrogen Abstraction Barriers

Substrate	$\Delta E^‡$	$\Delta(E+ZPE)^‡$	$\Delta H^‡$	$\Delta G^‡$
CH_4[a]				
HS	26.69	22.76	22.55	31.74
LS	26.54	22.31	21.68	32.35
C_2H_6[b]				
HS	19.4			
LS	16.2			
CH_2=CH–CH_3[c]				
HS	13.53	10.63	10.92	21.21
LS	13.52	10.83	11.28	21.35
Camphor[d]				
HS	18.8			
LS	17.3			
Camphor[e]				
HS	18.0			
LS	20.2			

Notes:
[a]Ogliaro *et al.*[62].
[b]Yoshizawa *et al.*[111].
[c]De Visser *et al.*[105].
[d]Cohen *et al.*[76].
[e]Kamachi and Yoshizawa[49].

at least a good part of this entropic effect, due to restriction in the $^{2,4}TS_{H}$ species, will not contribute to the free-energy barrier. *Thus, the protein machinery that utilizes mobile water molecules absorbs much of the entropic cost of establishing a TS.* Therefore, the gas phase quantities that are more informative of the situation in the protein are not $\Delta G^{\ddagger}$ but $\Delta(E+ZPE)^{\ddagger}$ and $\Delta H^{\ddagger}$. However, a thorough discussion of this feature is impossible at the time of the writing of this manuscript and will have to await QM/MM calculations with real sampling and thermodynamic integration.

5.4. The Rebound Process: More Features than Meet the Eye

The iron-hydroxo intermediate that is formed during the bond activation step exists in two close-lying electromers[101], which differ in the oxidation state of the metal and porphyrin ligand. By reference to the orbital diagram in Figure 2.14, these electromers differ in the orbital occupancy of the d-block and porphyrin a_{2u} orbitals; the Por+•Fe^{III}OH electromer has close lying singlet and triplet $\pi^{*2}_{xz}\ \pi^{*1}_{yz}\ a_{2u}^{1}$ configurations, while the PorFe^{IV}OH state has a triplet $\pi^{*1}_{xz}\ \pi^{*1}_{yz}\ a_{2u}^{2}$ configuration. These two electromeric situations are close in energy, and small changes such as substituents on the porphyrin ring or replacement of the axial ligand can reverse their ordering[101]. Coupling with the alkyl radical leads to five states of the corresponding HS and LS $Por^{+\bullet}Fe^{III}OH/R^{\bullet}$ and $PorFe^{IV}OH/R^{\bullet}$ species. Indeed, gas phase calculations give as ground states either electromer, as for example found recently by Kamachi and Yoshizawa[49] for camphor hydroxylation, where the LS electromer was of the $Por^{+\bullet}Fe^{III}OH/R^{\bullet}$ variety, while the HS electromer was of the $PorFe^{IV}OH/R^{\bullet}$ variety. All the five states can in turn participate in rebound, and as was repeatedly found[62, 105] that the HS intermediates rebound with a significant barrier ($2 < \Delta E^{\ddagger}_{reb} \leq 6$ kcal mol^{-1}), while the LS intermediates rebound without a barrier past the orientation phase (Figure 2.17) that occurs by combined rotation of the alkyl and OH groups.

The origin of the rebound barrier on the HS surface was analyzed[62, 102, 113] and shown to result from the need to shift an electron from the alkyl radical to the heme and populate the high-lying $\sigma^{*}_{z^2}$ orbital; this orbital is antibonding in the Fe–S and Fe–O linkages (see Figure 2.14). In line with the population of the $\sigma^{*}_{z^2}$ orbital, both Fe–S and Fe–O bonds are seen from Figure 2.20 to undergo lengthening in the $^{4}TS_{reb}$ species (relative to the values in the iron-hydroxo radical clusters, shown below the TSs). This bond lengthening is the origin of the HS rebound barrier. By contrast, in the LS process, the electron, shifted from the alkyl radical, fills only low-lying orbitals, either the π^{*}_{xz} orbital of iron or the porphyrin a_{2u} orbital depending on electromeric identity (Fe^{III} or Fe^{IV}). The rate of the rebound process depends much on the electron donor

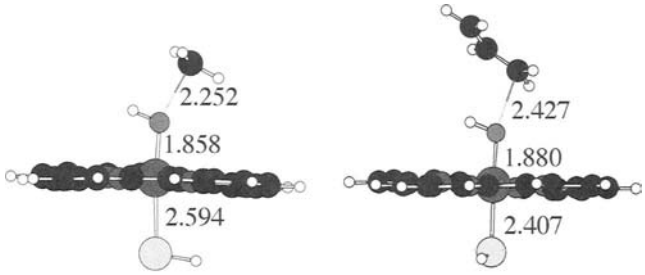

$^{4}TS_{reb}$; R = CH_3
r_{FeO} = 1.816
r_{FeS} = 2.480

$^{4}TS_{reb}$; R = C_3H_5
r_{FeO} = 1.804
r_{FeS} = 2.356

Figure 2.20. Key geometric parameters for high-spin rebound transition states in methane hydroxylation[62] and allylic hydroxylation[105]. The quantities below the structures correspond to the geometric parameters of the corresponding iron-hydroxo/alkyl radical clusters ($^{4}C_{1}$ in Figure 2.17).

capability of the radical and its C–O bond strength (see above), but also on the acceptor properties of the iron-hydroxo species, its electromeric state, and height of the $\sigma^*_{z^2}$ orbital; these properties depend on the polarity and acidity of the protein pocket and its steric constraints on the Fe–S bonding. The role of the $\sigma^*_{z^2}$ orbital was recently highlighted in the study of methane hydroxylation by the ruthenium analog of Cpd I (ref. [67]), where a very high $\sigma^*_{z^2}$ orbital led to a very high rebound barrier of *c.*11.9 kcal mol^{-1}. An additional factor revealed by the calculations[49, 105, 113] is that the rebound process may occur either by OH rotation around the Fe–O bond, as in the case of the methane monooxygenase enzyme[114], or by rotation of the alkyl group around the same bond, or still by some combination of the two modes. In allylic hydroxylation, the prominent mode was found to be the rotation of the allyl group about the Fe–OH bond[105], while in camphor hydroxylation, both OH and alkyl rotations take part in the rebound[49]. It is very clear that the topography of the protein pocket and the mode of substrate binding will play major roles in the rebound process, by selectively constraining/preferring some of the rebound modes over others. The results of Atkins and Sligar[82] that during camphor hydroxylation both *exo* and *endo* C–H bonds are activated, but the only product is an *exo*-alcohol, is indicative of the manifestations of such selective constraints. All in all, the rebound process is more intricate than meets the eye, and certainly more than QM or even QM/MM calculation can resolve at present. Here we have to look forward for a combination of QM/MM with MD calculations.

5.5. Alkene Epoxidation

The DFT (B3LYP/LACVP) computed mechanistic scheme for ethene epoxidation by the simplest model Cpd I species is summarized in Figure 2.21[97, 115, 116]. The first step involves bond activation and leads to the iron-alkoxy radical intermediate that appears in both Fe^{III} and Fe^{IV} electromers of the HS and LS varieties. In a subsequent phase, these intermediates undergo ring-closure to form the epoxide complex. The alternative synchronous concerted oxygen insertion was also tested[97] but ruled out as a viable mechanism. Precisely the same features were obtained for propene epoxidation[105], with the exception that the bond activation barriers are *c.*4 kcal mol^{-1} lower than those, shown in Figure 2.21, for ethene epoxidation.

The lowest energy TSs for bond activation for ethene and propene activation are shown in Figure 2.22. Since the bond activation involves an electron shift from the alkene to the heme (consult Figure 2.14), propene, which is a better electron donor than ethene, has lower barriers, 10.0 and 10.6 kcal mol^{-1} *vis-à-vis* 13.9 and 14.9 kcal mol^{-1} (HS, LS). In accord, the TSs of propene are seen to be earlier than those of ethene, with less C=C activation, etc. An interesting feature of the two

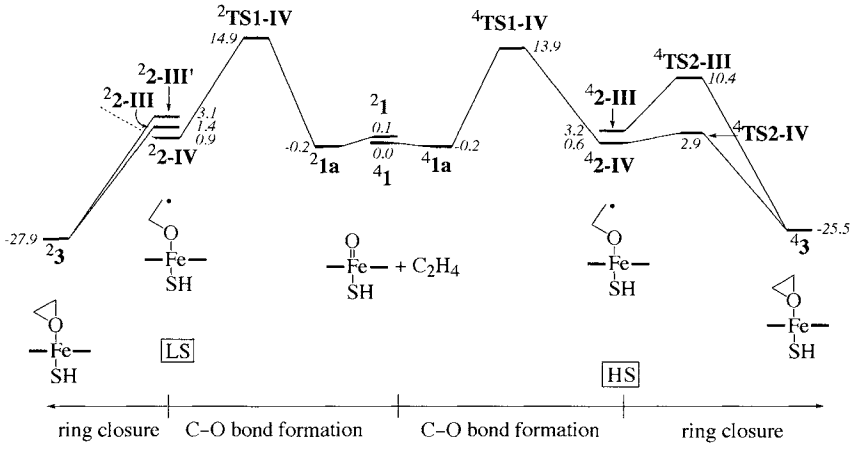

Figure 2.21. Two-state reactivity potential energy surface for ethene epoxidation[115].

TSs is their propensity for an upright orientation of the alkene moiety *vis-à-vis* the plane of the porphyrin. This gas phase conformation avoids the steric repulsion with the porphyrin. However, in the protein pocket, the upright conformation may encounter repulsion from the side-chain amino acids, and a compromise may be achieved in the parallel conformation, which is generated, in Figure 2.22, from the gas phase TS by a simple rotation that achieves a dihedral FeOCC angle of 90°. This structure is related to the one proposed by Groves *et al.*[117] to account for the preferred reactivity of *cis* compared with *trans* isomers, due to enhanced steric repulsion of the substituents in the latter isomer with the porphyrin ring (see the corresponding distances in Figure 2.22).

Past the bond activation phase, in Figure 2.21, the radicals undergo ring closure. As in the hydroxylation, the LS radical complexes undergo ring-closure in a virtually barrierless fashion, whereas on the HS surface, the radicals encounter significant barriers. These barriers for the HS Fe^{IV} electromer are smaller than those for rebound in alkane hydroxylation. However, the ring-closure barriers are large for the HS Fe^{III} electromers. This implies that the radical intermediate complexes, and especially those for the Fe^{III} electromer, will have a significant lifetime only on the HS surface, where they may give rise to rearranged products or lead to side reactions. For instance, rotations around the C–C or the C–O bonds were found to cost less than 1.5 kcal mol^{-1}. Thus, C–C rotation on the HS surface will result in the production

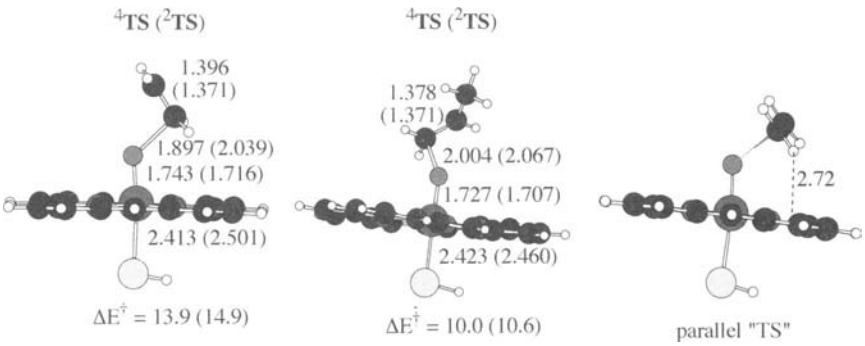

Figure 2.22. Computed structures of the C–O bond activation transition states, and barriers, for ethene[115] and propene epoxidation[105]. The putative "parallel" TS for ethene epoxidation is generated by rotating the computed one around the O–C bond.

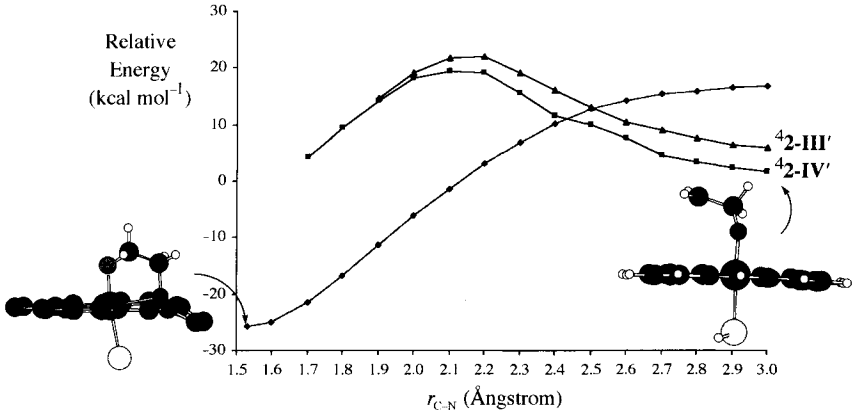

Figure 2.23. Geometry scan for the formation of the suicidal complex by crossover from the high-spin Fe^{III} intermediate (^{4}**2-III′**) to the state generated by promoting an electron from the methylene radical group to the σ^*_{xy} orbital of iron (see Figure 2.3).

of both *cis*-epoxide and *trans*-epoxides from *cis*- or *trans*-alkenes, whereas the LS surface will essentially retain the original isomeric identity of the alkene.

Similarly, rotation around the C–O is facile and will bring the radical center to a position for heme alkylation, where the alkylation barriers are small enough to compete with rebound. The DFT calculations[116] show that the HS radical complex of the Fe^{III} electromer can cross over to a state that is initially higher lying, but which is adiabatically connected with the suicidal complex in Figure 2.23. This crossing point is $\leq$10 kcal mol^{-1} above the Fe^{III} radical intermediate, so that this process may be able to compete with the ring closure of the Fe^{III} electromer to epoxide (with a barrier of 7.2 kcal mol^{-1}). The state, leading to the suicidal complex, is obtained by shifting an electron from the CH_2 moiety of the radical complex, which thereby becomes a carbocationic center, to the σ^*_{xy} orbital of the heme, which thereby becomes anionic with loose Fe–N bonds. As such, the state of the suicidal complex is an internal ion pair that undergoes cation (C^+) anion (N^-) combination, which is likely to be facilitated by the polar environment of the protein pocket. We have preliminary results for the mechanism of formation of the aldehyde side product, which is formed in a related mechanism to the suicidal complex[118]. The rebound barriers as well as those for the side product formation are subject to polarity and NH --- S hydrogen bonding effects[105].

5.6. Hydroxylation of Arenes

One of the long-standing controversies concerns the hydroxylation mechanism of arenes, which apart from phenol can produce also ketone and arene oxide as side products. A universal feature of arene-hydroxylation is the so-called NIH-shift, which accounts for the fact that the original hydrogen atom in the activated C–H bond is retained in the reaction products[1, 54]. A recent DFT investigation[119] addressed the mechanism of benzene hydroxylation. A rebound mechanism, analogous to alkane hydroxylation, and an electron transfer mechanism were ruled out due to their high-energy costs, while the lowest energy mechanisms were found to involve π-attack as summarized in Figure 2.24. In accord with deductions from experimental data[120, 121], the computations show that the bond activation proceeds via two mechanisms; one leads to a radical σ-complex ($^2\sigma$-C$^\bullet$) and the other to a cationic σ-complex

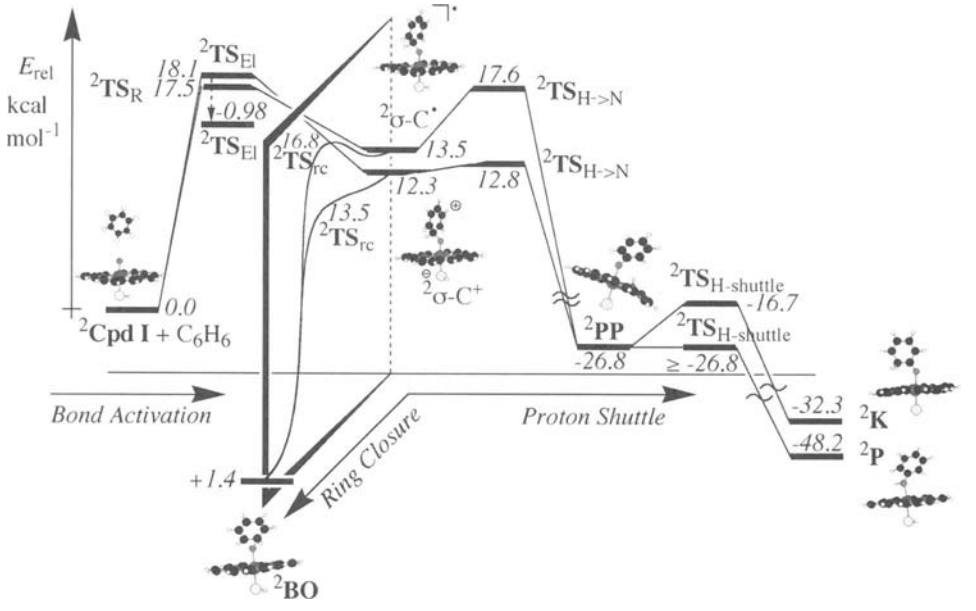

Figure 2.24. Potential energy surface for the competing oxidation mechanisms of benzene by Cpd I (ref. [119]).

($^2\sigma$-C+). Both the radical and electrophilic mechanisms involve the LS states, while the HS states give rise to TSs that are too high to compete with the LS states. Polarity and NH---S hydrogen bonding prefer the electrophilic pathway compared with the radical one. Thus, the calculations predict that the major pathway for arene hydroxylation will be the electrophilic pathway.

The so-formed intermediates, in Figure 2.24, subsequently bifurcate either to the ferric benzene oxide (^{2}**BO**) complex by ring closure, or to the N-protonated porphyrin intermediate (^{2}**PP**) by proton transfer from the *ipso* carbon to one of the nitrogens of the porphyrin. In turn, the latter intermediate reshuttles the proton either to the oxo group to give phenol (^{2}**P**) or to the *ortho* carbon to give the ketone (^{2}**K**). Since both $\mathbf{TS}_{H}$-shuttle species lie well below $\mathbf{TS}_{H->N}$, the excess energy will give rise to both phenol and ketone. This proton-shuttle mechanism accounts for the NIH-shift, since the original hydrogen in the activated C–H bond ends up in the products. It follows therefore that, in addition to phenol production by nonenzymatic protonation of benzene oxide under physiological condition, there should exist an enzymatic pathway that leads directly to phenol and ketone production without the intermediacy of benzene oxide.

5.7. Sulfoxidation of Alkyl Sulfides

Another common reaction of P450 is the sulfoxidation of sulfides[1]. Figure 2.25 summarizes the results of a recent DFT study of the sulfoxidation reaction of dimethyl sulfide with a Cpd I model[122]. The reaction is seen to proceed in a concerted manner via LS and HS pathways. However, in contrast to the hydroxylation of benzene[119], which occurs by a dominant LS potential energy surface, sulfoxidation exhibits a dominant HS pathway, which becomes even more so by inclusion of the effect of medium polarity (using a dielectric constant, $\varepsilon = 5.7$). Unlike alkane hydroxylation and alkene epoxidation where the TSs are related in their electronic structures and differ in having ferro-, namely antiferromagnetic coupling of the three unpaired electrons, in sulfoxidation, the LS and HS TSs are very different in their geometries and electronic structures because the two oxidation equivalents (Figure 2.14) must be condensed into a single step. Thus, sulfoxidation behaves as HS and LS displacement reactions where the sulfur attacks the oxo moiety and displaces the heme, which in turn rebinds to the sulfoxide via a long Fe–O bond. Different heme-oxo orbitals figure in the

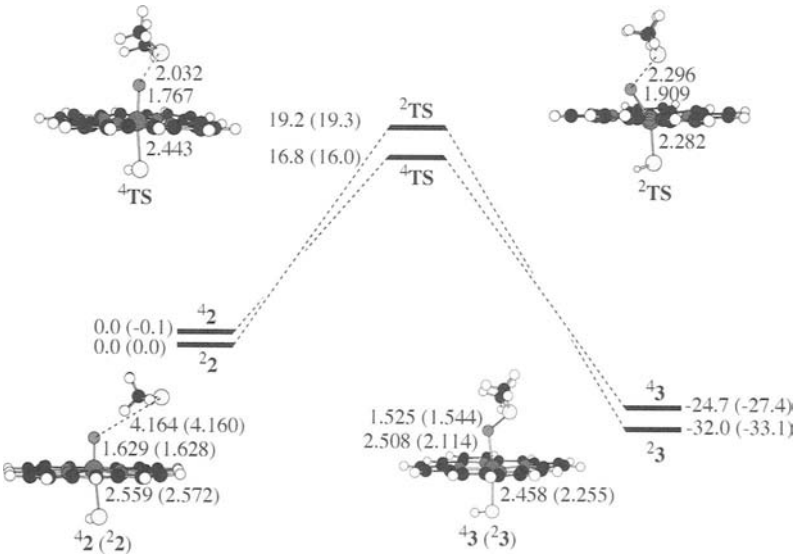

Figure 2.25. Potential energy surface for the sulfoxidation of dimethyl sulfide by Cpd I (ref. [122]). Barriers in parentheses incorporate the effect of a dielectric constant, $\varepsilon = 5.7$.

interaction with the lone pair of the attacking sulfur; in the LS process, these are the π^*(FeO) and a_{2u} orbitals that get filled up during the displacement, whereas in the HS process, the $\sigma^*_{z^2}$ and a_{2u} orbitals accept each one electron through the interaction with the sulfur. It seems reasonable to expect that the sulfoxidation results apply to other heteroatom oxidation processes. Our calculations, done for a single substrate, do not rule out an electron transfer mechanism for substrates that are more powerful donors. However, as a rule, the cysteine ligand makes Cpd I of P450 a relatively poor electron acceptor to participate in pure electron transfer processes with diffusive products[40].

5.8. Can Ferric Peroxide (6) be a Second Oxidant?

This question was addressed by the Jerusalem group using the marker reaction of Cpd 0: alkene epoxidation[53]; ethene served as the alkene. Four different mechanisms were computed, corresponding to concerted and stepwise epoxidations by both distal and proximal oxygen groups of Cpd 0. The barriers for the four mechanisms relative to those obtained by Cpd I that are displayed in Figure 2.26, show that Cpd 0 is by far inferior to Cpd I.

Similar results were obtained for sulfoxidation[122], where Cpd 0 led to barriers in excess of 40 kcal mol^{-1}, more than 20 kcal mol^{-1} higher than the barriers calculated for sulfoxidation by Cpd I. Hydrogen bonding (to an H_2O molecule) or simultaneous protonation (using a cluster of H_3O^+ and H_2O) and oxygen insertion processes were attempted too, and led to barriers which are at least 10 kcal mol^{-1} higher than those by Cpd I[122]. These results clearly show that by itself, Cpd 0 cannot possibly compete with Cpd I because the negative charge makes it a good base and a good nucleophile, but not an electrophile[53]. Its activation by a proton source improves the situation[122], but even then it appears that the Cpd 0 is a much poorer oxidant than Cpd I.

5.9. Competitive Hydroxylation and Epoxidation in Propene

The competition between C–H hydroxylation and C=C epoxidation for a given substrate was addressed[104, 105] using propene as a model. The reaction profiles for in-vacuum conditions are shown in Figure 2.27, which exhibit the already known features of TSR with effectively concerted LS pathways and stepwise HS mechanisms. First, the barriers are seen to be extremely small and they get even smaller when NH---S hydrogen bonding is included (e.g., the barrier for the LS hydroxylation becomes *c.*8.96 kcal mol^{-1} only). With these small barriers, we may anticipate that the substrate binding will control the regioselectivity, so that whichever moiety is bound to Cpd I will be the one to react, and will do so too fast to allow the observation of the competing reaction. Indeed, propene undergoes exclusive epoxidation

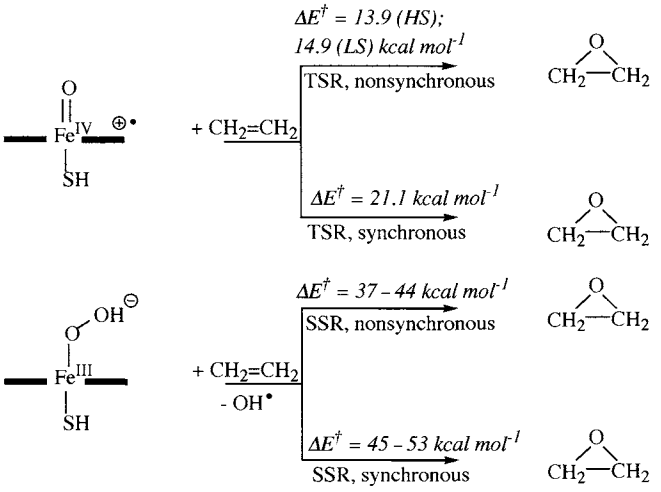

Figure 2.26. Epoxidation barriers of ethene by Cpd I and Cpd 0 (refs [53, 115]).

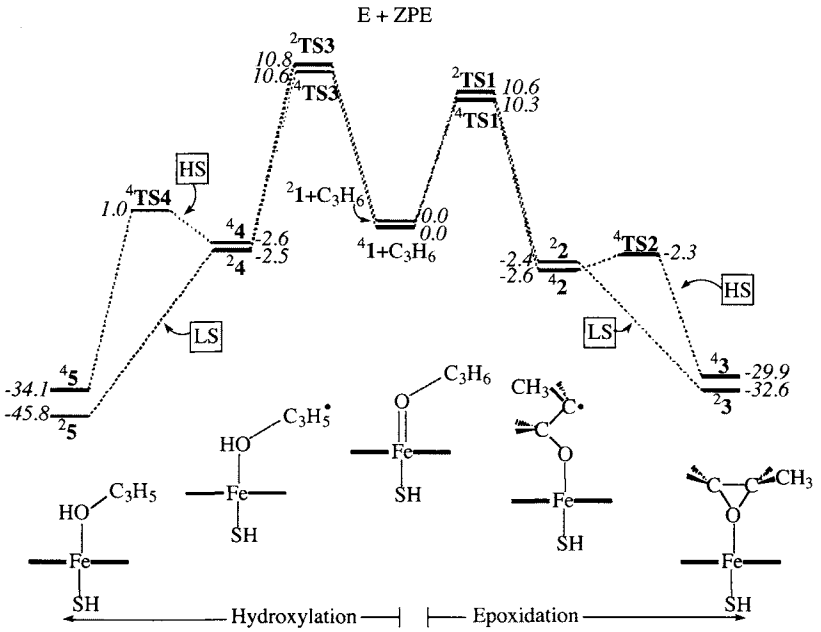

Figure 2.27. Potential energy landscape for the hydroxylation and epoxidation pathways of propene in the gas phase[105]. Relative energies include zero point energies (ZPE).

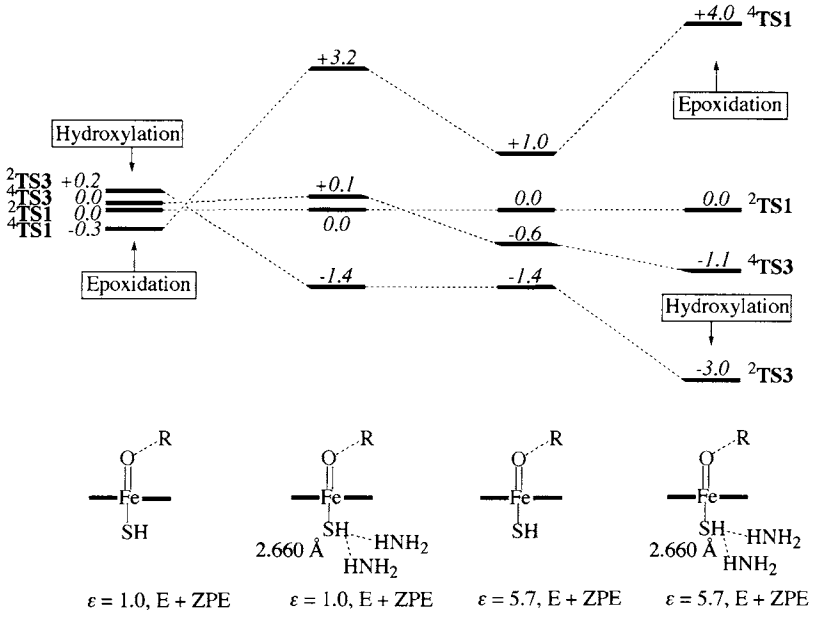

Figure 2.28. Relative energy of the transition states (TSs) for hydroxylation and epoxidation in the gas phase and under the influence of NH---S hydrogen bonding and polarity; the latter is mimicked by a dielectric constant $\varepsilon = 5.7$ (adapted from ref. [104, 105] with permission).

with $P450_{LM2}$ (ref. [123]), but this is not the case for other simple alkenes, for example, cyclohexene[124]. As such, our results with propene should be regarded as a model study of factors affecting regioselectivity and stereoselectivity rather than a specific study of a given substrate. In this respect, the calculations show that the bond activation phase is the rate-limiting step for both processes.

Figure 2.28 displays the four-bond activation TSs under different conditions. In the gas phase, the four species are condensed within 0.6 kcal mol^{-1}, with a slight preference for the epoxidation species. This in turn means that the gas phase reaction will exhibit (a) a low regioselectivity of C=C over C–H and (b) low stereospecificity due to HS/LS scrambling. The addition of just two NH --- S hydrogen bonds is sufficient to render the LS hydroxylation TS the lowest one by a wide margin. Adding the effect of a polar environment (mimicked by a dielectric constant of $\varepsilon = 5.7$) creates a clear preference for hydroxylation over epoxidation, by 3.0 kcal mol^{-1}. In addition, for each process, now the LS pathway has a lower barrier than the HS pathway. These effects correspond to a regioselectivity reversal by almost three orders of magnitude in favor of hydroxylation. In addition, since these effects favor the LS pathways, they also induce improvement in the stereoselectivity of both hydroxylation and epoxidation by almost three orders of magnitude. It follows therefore that the factors that mimic the polarity of the protein pocket and its hydrogen-bonding machinery have a major impact on the selectivity patterns of Cpd I. In fact, since Cpd I is a chameleon species, it also acts as a chameleon oxidant that tunes its reactivity patterns in response to the polarity and hydrogen-bonding machinery of the protein pocket. Thus, along with substrate binding, the hydrogen-bonding machinery and polarity of the protein serve as means by which the enzyme tunes its selectivity. One wonders whether this factor would not play a role in the great versatility of the superfamily of P450 enzymes.

5.10. An Overview of Reactivity Features of Cpd I

Cpd I *is a chameleon and two-state oxidant* and as such exhibits TSR that can be tuned by the polarity of the pocket and its hydrogen-bonding machinery. The gas phase (in vacuum) calculations show that, while alkane hydroxylation and alkene epoxidation feature TSR, by contrast, benzene hydroxylation exhibits a dominant LS reactivity and in sulfoxidation it is the HS state that dominates reactivity. As a rule of thumb, we may say that whenever the substrate deformation is small or identical for the two states, they will have similar electronic structures and be energetically close, as for the reactant species Cpd I. This appears to be the case in epoxidation and hydroxylation, which exhibit clear TSR. The dominance of the LS state in benzene hydroxylation was shown[119] to originate in the large deformation energy of benzene, due to the partial loss of the resonance energy, which is *c.*10 kcal mol^{-1} more severe for the HS TSs. In heteroatom oxidation, however, the electronic structures during the HS and LS processes are not the same since the two oxidation equivalents must be condensed into a single step, and for sulfoxidation, the HS state appears to be the lower one of the two. We may therefore anticipate that arene hydroxylation and heteroatom oxidation will feature a SSR with a substrate-dependent spin-state selection.

A feature encountered during benzene hydroxylation is the appearance of both radical and cationic mechanisms. This feature is associated with the stability of the cationic species and will appear in alkane hydroxylation and alkene epoxidation whenever the corresponding radical center has a sufficiently low ionization energy to transfer an electron to the heme. In such an event, the reactivity will be dominated by the LS state. The result of Newcomb and Toy[91], which indicates the presence of carbocations may well belong to this category. Such results are in progress.

The polarity of the pocket and hydrogen-bonding machinery were found to increase the dominance of the LS reactivity in arene hydroxylation and the HS reactivity in sulfoxidation. Similarly, these factors will have a strong impact on the appearance of cationic intermediates during hydroxylation and epoxidation. More intriguing is the result that these properties of the protein pocket have a major impact on the regioselectivity of C–H hydroxylation versus C=C epoxidation as well as on the stereospecificity of both processes. Time will show whether these are generalities or isolated findings.

Theory also shows that the porphyrin ring is not a spectator ligand but plays quite a few roles during the enzymatic reaction. It acts as an electron sink by accepting the excess electrons generated during the oxidation, and as a proton sponge by reshuttling protons needed for substrate rearrangement. These are in addition to its adverse role in enabling heme alkylation. In our calculations, we find that heme alkylation is more facile with ligands that are not good electron donors as the thiolate is. Thus, the thiolate ligand protects the porphyrin against heme alkylation, and at the same time, renders its nitrogen more basic and, hence, improves its catalytic performance as a proton shuttle.

6. Prospective

As shown in this chapter, theoretical treatments of P450 problems have come of age, and they enable the study of many features related to the three-dimensional structures, the electronic structures, substrate binding, reactivity, and dynamics of the various physical processes in the cycle. This ability will only increase with time, as the various techniques will be brought to bear simultaneously on a given problem. Techniques similar to combinatorial synthesis will have to be adopted in order to screen fast many alternative possibilities.

At present, while calculations have elucidated some important features of the cycle, still others remain obscure; especially features which concern the protein machinery and the dynamics of the various reactions, the role of the water molecules that are present in the pocket and leave it upon entrance of the substrate, and the dialogue between the oxygenase and the reductase domains, as well as the thermodynamic aspects of the entire cycle which must be determined by accounting for the changes in the reductase.

Other outstanding issues that remain unattended at present are the following:

(1) The role of spin crossover in the various events in the cycle, including the TSR during oxygenation, which will have to be elucidated.

(2) All calculations of C–H hydroxylation, with the exception of allylic hydroxylation, show a significant barrier of 18–24 kcal mol^{-1}. Such barriers seem to be overestimated. If this is a fault of the theoretical calculations, this is likely to be discovered as soon as calculations become faster and allow the use of more sophisticated methods (e.g., CCSD(T), CASPT2). If however, these are reasonable estimates of the barrier, we will be facing a conceptual dilemma to explain the potency of the enzyme despite the large barriers. While a few such possible scenarios come to mind immediately, we prefer to leave these as open questions that advanced theory will have to deal with in the future.

Acknowledgment

Sason Shaik's research was supported by ISF and GIF grants.

References

1. Ortiz de Montellano, P.R. (ed.), (1995). *Cytochrome P-450: Structures, Mechanism and Biochemistry*, 2nd edn. Plenum Press, New York.
2. Loew, G.H., C.J. Kert, L.M. Hjelmeland, and R.F. Kirchner (1977). Active site models of horseradish peroxidase compound I and a cytochrome P450 analogue: Electronic structure and electric field gradients. *J. Am. Chem. Soc.* **99**, 3534–3536.
3. Cramer, C.J. (2002). *Essentials of Computational Chemistry: Theories and Models*. Wiley, Chichester.
4. Ghosh, A. and P.R. Taylor (2003). High-level *ab initio* calculations on the energies of low-lying spin states of biologically relevant transition metal complexes: A first progress report. *Curr. Opin. Chem. Biol.* **7**, 113–124.
5. Lüdemann, S.K., V. Lounnas, and R.C. Wade (2000). How do substrates enter and products exit the buried active site of cytochrome P450cam? 1. Random expulsion molecular dynamics investigation of ligand access channels and mechanisms. *J. Mol. Biol.* **303**, 797–811.
6. Lüdemann, S.K., V. Lounnas, and R.C. Wade (2000). How do substrates enter and products exit the buried active site of cytochrome P450cam? 2. Steered molecular dynamics and adiabatic mapping of substrate pathways. *J. Mol. Biol.* **303**, 813–830.
7. Hermans, J. and L. Wang (1997). Inclusion of loss of translational and rotational freedom in theoretical estimates of free energies of binding. Application to a complex of benzene and mutant T4 lysozyme. *J. Am. Chem. Soc.* **119**, 2707–2714.

8. Kairys, V. and M.K. Gilson (2002). Enhanced docking with the mining minima optimizer: Acceleration and side-chain flexibility. *J. Comput. Chem.* **23**, 1656–1670.
9. Davydov, R., T.M. Makris, V. Kofman, D.E. Werst, S.G. Sligar, and B.M. Hoffman (2001). Hydroxylation of camphor by reduced oxy-cytochrome P450cam: Mechanistic implications of EPR and ENDOR studies of catalytic intermediates in native and mutant enzymes. *J. Am. Chem. Soc.* **123**, 1403–1415.
10. Hata, M., T. Hoshino, and M. Tsuda (2000). An ultimate species in the substrate oxidation process by cytochrome P-450. *Chem. Comm.* 2037–3038.
11. Du, P., F.U. Axe, G.H. Loew, S. Canuto, and M.C. Zerner (1991). Theoretical study on the electronic spectra of model Compound II complexes of peroxidases. *J. Am. Chem. Soc.* **113**, 8614–8621.
12. Kuramochi, H., L. Noodleman, and D.A. Case (1997). Density functional study on the electronic structures of model peroxidase compounds I and II. *J. Am. Chem. Soc.* **119**, 11442–11451.
13. Dawson, J.H., R.H. Holm, J.R. Trudell, G. Barth, R.E. Linder, E. Bunnenberg *et al.* (1976). Oxidized cytochrome P-450. Magnetic circular dichroism evidence for thiolate ligation in the substrate-bound form. Implications for the catalytic mechanism. *J. Am. Chem. Soc.* **98**, 3707–3709.
14. Poulos, T.L. (1996). The role of the proximal ligand in heme enzymes. *J. Biol. Inorg. Chem.* **1**, 356–359.
15. Schlichting, I., J. Berendzen, K. Chu, A.M. Stock, S.A. Maves, D.E. Benson *et al.* (2000). The catalytic pathway of cytochrome P450cam at atomic resolution. *Science* **287**, 1615–1622.
16. Loew, G.H. and D.L. Harris (2000). Role of the heme active site and protein environment in structure, spectra, and function of the cytochrome P450s. *Chem. Rev.* **100**, 407–419.
17. Loew, G.H. (2000). Structure, spectra, and function of heme sites. *Int. J. Quantum Chem.* **77**, 54–70.
18. Giler, A.H. and T. Clark (2001). SAM1 semiempirical calculations on the mechanism of cytochrome P450 metabolism. *Theochem.* **541**, 263–281.
19. Schöeboom, J.C., H. Lin, N. Reuter, W. Thiel, S. Cohen, F. Ogliaro *et al.* (2002). The elusive oxidant species of cytochrome P450 enzymes: Characterization by combined quantum mechanical/molecular mechanical (QM/MM) calculations. *J. Am. Chem. Soc.* **124**, 8142–8151.
20. Miyahara, T., Y. Tokita, and H. Nakatsuji (2001). SAC/SAC-CI study of the ground, excited, and ionized states of cytochromes P450CO. *J. Phys. Chem. B* **105**, 7341–7352.
21. Ghosh, A. and T. Wondimagegn (2000). A theoretical study of axial tilting and equatorial asymmetry in metalloporphyrin-nitrosyl complexes. *J. Am. Chem. Soc.* **122**, 8101–8102.
22. Wondimagegn, T. and A. Ghosh (2001). A quantum chemical survey of metalloporphyrin-nitrosyl linkage isomers: Insights into the observation of multiple FeNO conformations in a recent crystallographic determination of nitrophorin 4. *J. Am. Chem. Soc.* **123**, 5680–5683.
23. Ghosh, A. (1998). First-principles quantum chemical studies of porphyrins. *Acc. Chem. Res.* **31**, 189–198.
24. Ghosh, A., J. Almlöf, and L. Que Jr. (1994). Density functional theoretical study of oxo(porphyrinato) iron(IV) complexes, models of peroxidase Compounds I and II. *J. Phys. Chem.* **98**, 5576–5579.
25. Ghosh, A. and E. Gonzalez (2000). Theoretical studies on high-valent manganese porphyrins: Toward a deeper understanding of the energetics, electron distributions, and structural features of the reactive intermediates of enzymatic and synthetic manganese-catalyzed oxidative processes. *Isr. J. Chem.* **40**, 1–8.
26. Harris, D.L. and G.H. Loew (1998). Theoretical investigation of the proton assisted pathway to formation of cytochrome P450 compound I. *J. Am. Chem. Soc.* **120**, 8941–8948.
27. Filizola, M. and G.H. Loew (2000). Role of protein environment in horseradish peroxidase compound I formation: Molecular dynamics simulations of horseradish peroxidase-HOOH complex. *J. Am. Chem. Soc.* **122**, 18–25.
28. Loew, G.H. and M. Dupuis (1996). Structure of a model transient peroxide intermediate of peroxidases by ab initio methods. *J. Am. Chem. Soc.* **118**, 10584–10587.
29. Thomann, H., M. Bernardo, D. Goldfarb, P.M.H. Kroneck, and V. Ullrich (1995). Evidence for water binding to the Fe-center in cytochrome P450cam obtained by ^{17}O electron spin echo envelope modulation spectroscopy. *J. Am. Chem. Soc.* **117**, 8243–8251.
30. Collins, J.R., P. Du, and G.H. Loew (1992). Molecular dynamics simulations of the resting and hydrogen peroxide-bound states of cytochrome c peroxidase. *Biochemistry* **31**, 11166–11174.
31. Harris, D.L. and G.H. Loew (1993). Mechanistic origin of the correlation between spin state and spectra of model cytochrome P450 ferric heme proteins. *J. Am. Chem. Soc.* **115**, 5799–5802.
32. Harris, D.L. and G.H. Loew (1993). Determinants of the spin state of the resting state of cytochrome P450cam. *J. Am. Chem. Soc.* **115**, 8775–8779.
33. Aissaoui, H., R. Bachmann, A. Schweiger, and W.-D. Woggon (1998). On the origin of the low-spin character of cytochrome P450cam in the resting state-investigations of enzyme models with

pulse EPR and ENDOR spectroscopy. *Angew. Chem. Int. Ed.* **37**, 2998–3002.
34. Green, M.T. (1998). Role of the axial ligand in determining the spin state of resting cytochrome P450. *J. Am. Chem. Soc.* **120**, 10772–10773.
35. Filatov, M., N. Harris, and S. Shaik (1999). A theoretical study of electronic factors affecting hydroxylation by model ferryl complexes of cytochrome P-450 and horseradish peroxidase. *J. Chem. Soc. Perkin Trans. 2*, 399–410.
36. De Visser, S.P., D. Kumar, S. Cohen, P.K. Sharma, and S. Shaik (2004, in preparation). A theoretical investigation of the proton-relay mechanisms for the formation of Cpd 0 and Cpd I in the catalytic cycle of cytochrome P450.
37. Scherlis, D.A., C.B. Cymeryng, and D.A. Estrin (2000). Nitric oxide binding to ferric cytochrome P450: A computational study. *Inorg. Chem.* **39**, 2352–2359.
38. Scherlis, D.A., M.A. Martí P. Ordejó, and D.A. Estrin (2002). Environment effects on chemical reactivity of heme proteins. *Int. J. Quantum Chem.* **90**, 1505–1514.
39. Loew, G.H. and M. Dupuis (1997). Characterization of a resting state model of peroxidases by ab initio methods: Optimized geometries, electronic structures, and relative energies of the sextet, quartet, and doublet spin states. *J. Am. Chem. Soc.* **119**, 9848–9851.
40. Ogliaro, F., S.P. De Visser, and S. Shaik (2002). The "push" effect of the thiolate ligand in cytochrome P450: A theoretical gauging. *J. Inorg. Biochem.* **91**, 554–567.
41. Sligar, S.G. (1976). Coupling of spin, substrate, and redox equilibria in cytochrome P450. *Biochemistry* **15**, 5399–5406.
42. Auclair, K., P. Moënne-Loccoz, and P.R. Ortiz de Montellano (2001). Role of the proximal heme thiolate ligand in cytochrome P450cam. *J. Am. Chem. Soc.* **123**, 4877–4885.
43. Yamamoto, S. and H. Kashiwagi (1989). CASSCF study on the Fe–O_2 bond in a dioxygen heme complex. *Chem. Phys. Lett.* **161**, 85–89.
44. Harris, D.L., G.H. Loew, and L. Waskell (1998). Structure and spectra of ferrous dioxygen and reduced ferrous dioxygen model cytochrome P450. *J. Am. Chem. Soc.* **120**, 4308–4318.
45. Chottard, G., M. Schappacher, L. Ricard, and R. Weiss (1984). Resonance Raman spectra of iron(II) cytochrome P450 model complexes: Influence of the thiolate ligand. *Inorg. Chem.* **23**, 4557–4561.
46. Harris, D.L. and G.H. Loew (1994). A role for Thr252 in cytochrome P450cam oxygen activation. *J. Am. Chem. Soc.* **116**, 11671–11674.
47. Harris, D.L. and G.H. Loew (1996). Investigation of the proton-assisted pathway to formation of the catalytically active, ferryl species of P450s by molecular dynamics studies of P450eryF. *J. Am. Chem. Soc.* **118**, 6377–6387.
48. Guallar, V., D.L. Harris, V.S. Batista, and W.H. Miller (2002). Proton-transfer dynamics in the activation of cytochrome P450eryF. *J. Am. Chem. Soc.* **124**, 1430–1437.
49. Kamachi, T. and K. Yoshizawa (2003). A theoretical study on the mechanism of camphor hydroxylation by compound I of cytochrome P450. *J. Am. Chem. Soc.* **125**, 4652–4661.
50. Aikens, J. and S.G. Sligar (1994). Kinetic solvent isotope effects during oxygen activation by cytochrome P-450cam. *J. Am. Chem. Soc.* **116**, 1143–1144.
51. Harris, D.L. (2002). Oxidation and electronic state dependence of proton transfer in the enzymatic cycle of cytochrome P450eryF. *J. Inorg. Biochem.* **91**, 568–585.
52. Vidakovic, M., S.G. Sligar, H. Li, and T.L. Poulos (1998). Understanding the role of the essential Asp251 in cytochrome P450cam using site-directed mutagenesis, crystallography, and kinetic solvent isotope effect. *Biochemistry* **37**, 9211–9219.
53. Ogliaro, F., S.P. De Visser, S. Cohen, P.K. Sharma, and S. Shaik (2002). Searching for the second oxidant in the catalytic cycle of cytochrome P450: A theoretical investigation of the iron(III)-hydroperoxo species and its epoxidation pathways. *J. Am. Chem. Soc.* **124**, 2806–2817.
54. Sono, M., M.P. Roach, E.D. Coulter, and J.H. Dawson (1996). Heme-containing oxygenases. *Chem. Rev.* **96**, 2841–2887.
55. Yamamoto, S., J. Teraoka, and H. Kashiwagi (1988). Ab initio RHF and CASSCF studies on Fe–O bond in high-valent iron-oxo porphyrins. *J. Chem. Phys.* **88**, 303–312.
56. Harris, D.L., G.H. Loew, and L. Waskell (2001). Calculation of the electronic structure and spectra of model cytochrome P450 compound I. *J. Inorg. Biochem.* **83**, 309–318.
57. Ogliaro, F., S. Cohen, M. Filatov, N. Harris, and S. Shaik (2000). The high-valent compound of cytochrome P450: The nature of the Fe–S bond and the role of the thiolate ligand as an internal electron donor. *Angew. Chem. Int. Ed.* **39**, 3851–3855.
58. Ogliaro, F., S.P. De Visser, S. Cohen, J. Kaneti, and S. Shaik (2001). The experimentally elusive oxidant of cytochrome P450: A theoretical "trapping" defining more closely the "real" species. *Chembiochem.* **2**, 848–851.
59. Antony, J., M. Grodzicki, and A.X. Trautwein (1997). Local density functional study of oxo-iron(IV) porphyrin complexes and their one-electron oxidized derivatives. Axial ligand effects. *J. Phys. Chem. A* **101**, 2692–2701.

60. Green, M.T. (1999). Evidence for sulfur-based radicals in thiolate compound I intermediates. *J. Am. Chem. Soc.* **121**, 7939–7940.
61. Ohta, T., K. Matsuura, K. Yoshizawa, and I. Morishima (2000). The electronic and vibrational structures of iron-oxo porphyrin with a methoxide or cysteinate axial ligand. *J. Inorg. Biochem.* **82**, 141–152.
62. Ogliaro, F., N. Harris, S. Cohen, M. Filatov, S.P. De Visser, and S. Shaik (2000). A model "rebound" mechanism of hydroxylation by cytochrome P450: Stepwise and effectively concerted pathways, and their reactivity patterns. *J. Am. Chem. Soc.* **122**, 8977–8989.
63. Ogliaro, F., S. Cohen, S.P. De Visser, and S. Shaik (2000). Medium polarization and hydrogen bonding effects on compound I of cytochrome P450: What kind of a radical is it really? *J. Am. Chem. Soc.* **122**, 12892–12893.
64. Rutter, R., L.P. Hager, H. Dhonau, M. Hendrich, M. Valentine, and P. Debrunner (1984). Chloroperoxidase compound I: Electron paramagnetic resonance and Mössbauer studies. *Biochemistry* **23**, 6809–6816.
65. De Visser, S.P., F. Ogliaro, Z. Gross, and S. Shaik (2001). What is the difference between the manganese porphyrin and corrole analogues of cytochrome P450's compound I? *Chem. Eur. J.* **7**, 4954–4960.
66. Ogliaro, F., S.P. De Visser, J.T. Groves, and S. Shaik (2001). Chameleon states: High-valent metal-oxo species of cytochrome P450 and its ruthenium analogue. *Angew. Chem. Int. Ed.* **40**, 2874–2878.
67. Sharma, P.K., S.P. De Visser, F. Ogliaro, and S. Shaik (2003). Is the ruthenium analog of compound I of cytochrome P450 an efficient oxidant? A theoretical investigation of the methane hydroxylation reaction. *J. Am. Chem. Soc.* **125**, 2291–2300.
68. Green, M.T. (2000). Imidazole-ligated compound I intermediates: The effects of hydrogen bonding. *J. Am. Chem. Soc.* **122**, 9495–9499.
69. Green, M.T. (2001). The structure and spin coupling of catalase compound I: A study of noncovalent effects. *J. Am. Chem. Soc.* **123**, 9218–9219.
70. Deeth, R.J. (1999). Saddle distortions of ferryl-porphyrin models for peroxidase compound I: A density functional study. *J. Am. Chem. Soc.* **121**, 6074–6075.
71. Ogliaro, F. and S. Shaik (2003). Substituent effects on structure and properties of compound I species. Unpublished results.
72. Wirstam, M., M.R.A. Blomberg, and P.E.M. Siegbahn (1999). Reaction mechanism of compound I formation in heme peroxidases: A density functional theory study. *J. Am. Chem. Soc.* **121**, 10178–10185.
73. Lewis, D.F.V. (2001). *Guide to Cytochromes P450.* Taylor and Francis, New York.
74. Poulos, T.L., B.C. Finzel, and A.J. Howard (1986). Crystal structure of substrate-free *Pseudomonas putida* Cytochrome P450. *Biochemistry* **25**, 5314–5322.
75. Mueller, E.J., P.J. Loida, and S.G. Sligar (1995). Twenty-five years of P450cam research. In P.R. Ortiz de Montellano (ed.), *Cytochrome P-450: Structures, Mechanism and Biochemistry*, 2nd edn. pp. 83–124. Plenum Press, New York.
76. Schöneboom, J.C., S. Cohen, H. Lin, S. Shaik, and W. Thiel (2004). Quantum mechanical/molecular mechanical investigation of the mechanism of C-H hydroxylation of camphor by cytochrome $P450_{cam}$: Theory supports a two-state rebound mechanism. *J. Am. Chem. Soc.* **126**, 4017–4034.
77. Kesero G.M., I. Kolossváry, and B. Bertók (1997). Cytochrome P-450 catalyzed insecticide metabolism. Prediction of regio- and stereoselectivity in the primer metabolism of carbofuran: A theoretical study. *J. Am. Chem. Soc.* **119**, 5126–5131.
78. Kesero G.M., I. Kolossváry, and I. Szekely (1999). Inhibitors of cytochrome P450 catalyzed insecticide metabolism: A rational approach. *Int. J. Quantum Chem.* **73**, 123–135.
79. Cavalli, A. and M. Recanatini (2002). Looking for selectivity among cytochrome P450s inhibitors. *J. Med. Chem.* **45**, 251–254.
80. Lee, H., P.R. Ortiz de Montellano, and A.E. McDermott (1999). Deuterium magic angle spinning studies of substrates bound to cytochrome P450. *Biochemistry* **38**, 10808–10813.
81. De Voss, J.J., O. Sibbesen, Z. Zhang, and P.R. Ortiz de Montellano (1997). Substrate docking algorithms and prediction of the substrate specificity of cytochrome P450cam and its L244A mutant. *J. Am. Chem. Soc.* **119**, 5489–5498.
82. Atkins, W.M. and S.G. Sligar (1987). Metabolic switching in cytochrome P450cam: Deuterium isotope effects on regiospecificity and the monooxygenase/oxidase ratio. *J. Am. Chem. Soc.* **109**, 3754–3760.
83. Audergon, C., K.R. Iyer, J.P. Jones, J.F. Darbyshire, and W.F. Trager (1999). Experimental and theoretical study of the effect of active-site constrained substrate motion on the magnitude of the observed intramolecular isotope effect for the P450 101 catalyzed benzylic hydroxylation of isomeric xylenes and 4,4′-dimethylbiphenyl. *J. Am. Chem. Soc.* **121**, 41–47.
84. Helms, V. and R.C. Wade (1998). Hydration energy landscape of the active site cavity in cytochrome P450cam. *Proteins* **32**, 381–396.
85. Winn, P.J., S.K. Lüdemann, R. Gauges, V. Lounnas, and R.C. Wade (2002). Comparison of the

dynamics of substrate access channels in three cytochrome P450s reveals different opening mechanisms and a novel functional role for a buried arginine. *Proc. Natl. Acad. Sci. USA.* **99**, 5361–5366.
86. Das, B., V. Helms, V. Lounnas, and R.C. Wade (2000). Multicopy molecular dynamics simulations suggest how to reconcile crystallographic and product formation data for camphor enantiomers bound to cytochrome P-450cam. *J. Inorg. Biochem.* **81**, 121–131.
87. Fruetel, J.A., J.R. Collins, D.L. Camper, G.H. Loew, and P.R. Ortiz de Montellano (1992). Calculated and experimental absolute stereochemistry of the styrene and β-methylstyrene epoxides formed by cytochrome P450cam. *J. Am. Chem. Soc.* **114**, 6987–6993.
88. Harris, D.L. and G.H. Loew (1995). Prediction of regiospecific hydroxylation of camphor analogs by cytochrome P450cam. *J. Am. Chem. Soc.* **117**, 2738–2746.
89. Park, J.-Y. and D.L. Harris (2003). Construction and assessment of models of CYP2E1: Predictions of metabolism from docking, molecular dynamics and density functional theoretical calculations. *J. Med. Chem.* **46**, 1645–1660.
90. Vaz, A.D.N., D.F. McGinnity, and M.J. Coon (1998). Epoxidation of olefins by cytochrome P450: Evidence from site-specific mutagenesis for hydroperoxo-iron as an electrophilic oxidant. *Proc. Natl. Acad. Sci. USA.* **95**, 3555–3560.
91. Newcomb, M. and P.H. Toy (2000). Hypersensitive radical probes and the mechanisms of cytochrome P450-catalyzed hydroxylation reactions. *Acc. Chem. Res.* **33**, 449–455.
92. Jin, S., T.M. Markis, T.A. Bryson, S.G. Sligar, and J.H. Dawson (2003). Epoxidation of olefins by hydroperoxo-ferric cytochrome P450. *J. Am. Chem. Soc.* **125**, 3406–3407.
93. Shaik, S., M. Filatov, D. Schröder, and H. Schwarz (1998). Electronic structure makes a difference: Cytochrome P450 mediated hydroxylations of hydrocarbons as a two-state reactivity paradigm. *Chem. Eur. J.* **4**, 193–199.
94. Schröder, D., S. Shaik, and H. Schwarz (2000). Two-state reactivity as a new concept in organometallic chemistry. *Acc. Chem. Res.* **33**, 139–145.
95. Shaik, S., S.P. De Visser, F. Ogliaro, H. Schwarz, and D. Schröder (2002). Two-state reactivity mechanisms of hydroxylation and epoxidation by cytochrome P-450 revealed by theory. *Curr. Opin. Chem. Biol.* **6**, 556–567.
96. Sevin, A. and M. Fontecave (1986). Oxygen transfer from iron oxo porphyrins to ethylene. A semiempirical MO/VB approach. *J. Am. Chem. Soc.* **108**, 3266–3272.
97. De Visser, S.P., F. Ogliaro, and S. Shaik (2001). Stereospecific oxidation by Compound I of cytochrome P450 does not proceed in a concerted synchronous manner. *Chem. Comm.* 2322–2323.
98. Groves, J.T. and G.A. McClusky (1976). Aliphatic hydroxylation via oxygen rebound. Oxygen transfer catalyzed by iron. *J. Am. Chem. Soc.* **98**, 859–861.
99. Ortiz de Montellano, P.R. and R.A. Stearns (1987). Timing of the radical recombination step in cytochrome P450 catalysis with ring-strained probes. *J. Am. Chem. Soc.* **109**, 3415–3420.
100. Newcomb, M., R. Shen, S.-Y. Choi, P.H. Toy, P.F. Hollenberg, A.D.N. Vaz *et al.* (2000). Cytochrome P450-catalyzed hydroxylation of mechanistic probes that distinguish between radicals and cations. Evidence for cationic but not for radical intermediates. *J. Am. Chem. Soc.* **122**, 2677–2686.
101. Filatov, M., N. Harris, and S. Shaik (1999). On the "rebound" mechanism of alkane hydroxylation by cytochrome P450: Electronic structure of the intermediate and the electron transfer character in the rebound step. *Angew. Chem. Int. Ed.* **38**, 3510–3512.
102. Harris, N., S. Cohen, M. Filatov, F. Ogliaro, and S. Shaik (2000). Two-state reactivity in the rebound step of alkane hydroxylation by cytochrome P-450: Origins of free radicals with finite lifetimes. *Angew. Chem. Int. Ed.* **39**, 2003–2007.
103. Ogliaro, F., M. Filatov, and S. Shaik (2000). Alkane hydroxylation by cytochrome P450: Is kinetic isotope effect a reliable probe of transition state structure? *Eur. J. Inorg. Chem.* 2455–2458.
104. De Visser, S.P., F. Ogliaro, P.K. Sharma, and S. Shaik (2002). Hydrogen bonding modulates the selectivity of enzymatic oxidation by P450: Chameleon oxidant behavior by Compound I. *Angew. Chem. Int. Ed.* **41**, 1947–1951.
105. De Visser, S.P., F. Ogliaro, P.K. Sharma, and S. Shaik (2002). What factors affect the regioselectivity of oxidation by cytochrome P450? A DFT study of allylic hydroxylation and double bond epoxidation in a model reaction. *J. Am. Chem. Soc.* **124**, 11809–11826.
106. Cohen, S. and S. Shaik (2004). Quntum mechanical/molecular mechanical study of the regioselectivity of camphor and cyclohexene oxidations by cytochrome P450cam. In preparation; part of the Ph. D. thesis of Mrs. S. Cohen.
107. Yoshizawa, K. (2002). Theoretical study on kinetic isotope effects in the C–H bond activation of alkanes by iron-oxo complexes. *Coord. Chem. Rev.* **226**, 251–259.
108. Yoshizawa, K., T. Ohta, M. Eda, and T. Yamabe (2000). Two-step concerted mechanism for the hydrocarbon hydroxylation by cytochrome P450. *Bull. Chem. Soc. Jpn.* **73**, 401–407.
109. Yoshizawa, K., Y. Shiota, and Y. Kagawa (2000). Energetics for the oxygen rebound mechanism of alkane hydroxylation by the iron-oxo species of

cytochrome P450. *Bull. Chem. Soc. Jpn.* **73**, 2669–2673.

110. Yoshizawa, K., Y. Kagawa, and Y. Shiota (2000). Kinetic isotope effects in a C-H bond dissociation by the iron-oxo species of cytochrome P450. *J. Phys. Chem. B* **104**, 12365–12370.
111. Yoshizawa, K., T. Kamachi, and Y. Shiota (2001). A theoretical study of the dynamic behavior of alkane hydroxylation by a compound I model of cytochrome P450. *J. Am. Chem. Soc.* **123**, 9806–9816.
112. Hata, M., Y. Hirano, T. Hoshino, and M. Tsuda (2001). Monooxygenation mechanism by cytochrome P-450. *J. Am. Chem. Soc.* **123**, 6410–6416.
113. Shaik, S., S. Cohen, S.P. de Visser, P.K. Sharma, D. Kumar, S. Kozuchs *et al.* (2004). The "rebound controversy": An overview and theoretical modeling of the rebound step in C-H hydroxylaion by cytochrome P450. *Eur. J. Inorg. Chem.* 207–226.
114. Guallar, V., B.F. Gherman, W.H. Miller, S.J. Lippard, and R.A. Friesner (2002). Dynamics of alkane hydroxylation at the non-heme diiron center in methane monooxygenase. *J. Am. Chem. Soc.* **124**, 3377–3384.
115. De Visser, S.P., F. Ogliaro, N. Harris, and S. Shaik (2001). Multi-state epoxidation of ethene by cytochrome P450: A quantum chemical study. *J. Am. Chem. Soc.* **123**, 3037–3047.
116. De Visser, S.P., F. Ogliaro, and S. Shaik (2001). How does ethene inactivate cytochrome P450 en route to its epoxidation? A density functional study. *Angew. Chem. Int. Ed.* **40**, 2871–2874.
117. Groves, J.T., K.-H. Ahn, and R. Quinn (1988). Cis-trans isomerization of epoxides catalyzed by ruthenium(II) porphyrins. *J. Am. Chem. Soc.* **110**, 4217–4220.
118. De Visser, S.P., D. Kumar, and S. Shaik (2004). How do aldehyde side products occur during alkene epoxidation by cytochrome P450? Theory reveals a state-specific multi-state scenario where the high-spin component leads to all side products. *J. Inorg. Biochem.* in press.
119. De Visser, S.P. and S. Shaik (2003). A proton-shuttle mechanism mediated by the porphyrin in benzene hydroxylation by cytochrome P450 enzymes. *J. Am. Chem. Soc.* **125**, 7413–7424.
120. Korzekwa, K.R., D.C. Swinney, and W.F. Trager (1989). Isotopically labeled chlorobenzenes as probes for the mechanism of cytochrome P450 catalyzed aromatic hydroxylation. *Biochemistry* **28**, 9019–9027.
121. Rietjens, I.M.C.M., A.E.M.F. Soffers, C. Veeger, and J. Vervoort (1993). Regioselectivity of cytochrome P-450 catalyzed hydroxylation of fluorobenzenes predicted by calculated frontier orbital substrate characteristics. *Biochemistry* **32**, 4801–4812.
122. Sharma, P.K., S.P. de Visser, and S. Shaik (2003). Can a single oxidant with two-spin states masquerade as two different oxidants? A study of the sulfoxidation mechanism by cytochrome P450. *J. Am. Chem. Soc.* **125**, 8698–8699.
123. Groves, J.T., G.E. Avaria-Neisser, K.M. Fish, M. Imachi, and R.L. Kuczkowski (1986). Hydrogen-deuterium exchange during propylene epoxidation by cytochrome P450. *J. Am. Chem. Soc.* **108**, 3837–3838.
124. Groves, J.T. and D.V. Subramanian (1984). Hydroxylation by cytochrome P450 and metalloporphyrin models. Evidence for allylic rearrangement. *J. Am. Chem. Soc.* **106**, 2177–2181.